Spring 2024

Characterization of the Acquisition Parameters of a Submersible Gamma-Ray Computed Tomography System

Zhongmin Jin
Missouri University of Science and Technology

Department: Nuclear Engineering and Radiation Science

CHARACTERIZATION OF THE ACQUISITION PARAMETERS OF A SUBMERSIBLE GAMMA-RAY COMPUTED TOMOGRAPHY SYSTEM

by

ZHONGMIN JIN

A DISSERTATION

Presented to the Graduate Faculty of the

MISSOURI UNIVERSITY OF SCIENCE AND TECHNOLOGY

In Partial Fulfillment of the Requirements for the Degree

DOCTOR OF PHILOSOPHY

in

NUCLEAR ENGINEERING

2023

Approved by:

Joseph Graham, Advisor
Ayodeji Babatunde Alajo
Carlos H. Castano
Syed Alam
Monday Okoronkwo

PUBLICATION DISSERTATION OPTION

This dissertation consists of the following three articles, formatted in the style used by the Missouri University of Science and Technology:

Paper I, found on pages 23–47, has been published in *Nuclear Instruments and Methods in Physics Research A: Accelerators, Spectrometers, Detectors and Associated Equipment.*

Paper II, found on pages 48–61, has been submitted to *The Journal of Radioanalytical and Nuclear Chemistry.*

Paper III, found on pages 62–67, has been published in the Proceedings of the American Nuclear Society Conference in November 2020.

ABSTRACT

The purpose of this work is to study a component of a submersible gamma-ray computed tomography (CT) system used in the non-destructive testing of irradiated nuclear fuels. The first section of this study proposes two acceleration approaches for rapidly modeling a transmission-type gamma-ray tomography system. The first relies on Monte Carlo simulations with a monodirectionally biased source sampled from a sub-volume of the whole source volume. This method estimates the real count rate using analytical correction factors. The second way of acceleration is based on deterministic calculations that use the Beer-Lambert law and detector response characteristics. It shows that both results qualitatively agree with the analog result and can cut computational costs by several orders of magnitude. The second section of this study presents a novel approach for differentiating low-intensity, high-energy gamma rays in high-intensity, lower-energy backgrounds, particularly when the source is in a substantially scattering medium. Using a fast plastic scintillator and pulse-height discrimination, high-energy rays from low-activity ^{60}Co are differentiated from lower-energy rays of high-activity ^{137}Cs. By optimizing the discriminator voltage, the count time required to reach the limit of quantification (LOQ) is significantly reduced. This cost-effective solution utilizes commonly available lab equipment and improves detection efficiency.

ACKNOWLEDGMENTS

I would like to express my deepest gratitude to my dissertation committee members for their invaluable support and guidance throughout my research journey. I know, it's a long one. First and foremost, I am immensely grateful to my advisor, Dr. Joseph Graham, for his understanding, encouragement, and unwavering support when I am down and weary. His expertise and insights were instrumental in shaping the direction of my research, and I am fortunate to have had him as my advisor. I would also like to extend my sincere thanks to the other members of my committee: Dr. Ayodeji Babatunde Alajo, Dr. Carlos H. Castano, and Dr. Syed Alam. Each of them played a crucial role in my academic development, and I am grateful for the knowledge and skills I gained through their classes and seminars, which broadened my horizons and enriched my understanding of the field. I was deeply moved by Dr. Monday Okoronkwo's commitment to my research, as he took the time to provide valuable feedback on my research even during his vacation.

Finally, I would like to acknowledge my family and friends for their tremendous love and support. In particular, I want to thank my sister for her selfless sacrifices and tireless efforts in taking care of our family while I was thousands of miles away. Her dedication and commitment to our family has been a source of inspiration to me, and I could not have made it this far without her. Mom, Love you.

TABLE OF CONTENTS

Page

LIST OF ILLUSTRATIONS

SECTION Page

LIST OF TABLES

1. INTRODUCTION

Post-irradiation examination (PIE) is a method used to analyze and investigate the physical condition of nuclear fuel after it has been used in a reactor. It is a critical process in understanding the behavior of different materials under the extreme environment within a nuclear reactor [1, 2]. The data obtained from PIE is invaluable to nuclear scientists and engineers. It is used to validate and improve computer models that predict fuel behavior, confirm safety margins, improve fuel designs, and guide regulatory decisions. PIE may include various types of non-destructive testing (NDT) and destructive testing [3–20]. NDT techniques include visual inspection, eddy current testing, ultrasonic testing, and radiographic testing, which can reveal information about physical changes, defects, or damage that occurred during irradiation without breaching the cladding or otherwise altering the fuel. Destructive tests, on the other hand, involve cutting, sectioning, or otherwise altering the specimen to study things like microstructure, chemical composition, and fission product distribution. These tests provide more detailed information at the cost of destroying the sample.

1.1. NON-DESTRUCTIVE TESTING OF NUCLEAR FUEL

One of the challenges with post-irradiation fuel examination techniques is that they must be conducted in a shielded facility due to the high levels of radioactivity. Such facilities require specialized equipment and stringent safety protocols. NDT offers significant advantages in the context of nuclear fuels and plays a critical role in the nuclear fuel industry. As the nuclear industry continues to innovate and experiment with novel fuel

designs, the demand for accurate, efficient, and reliable NDT methods grows. Non-destructive imaging methods evaluate materials using highly penetrating radiation, such as neutrons, X-rays, or gamma rays. Researchers and inspectors can use these imaging techniques to analyze the structural integrity, internal structure, and performance of nuclear materials[21–43]. The following section provides an in-depth description of the three main NDT imaging techniques used in nuclear fuel analysis: neutron imaging, X-ray imaging, and gamma-ray imaging.

1.1.1. Neutron Imaging. Neutron imaging is an NDT for assessing the structural integrity and fissile content of nuclear fuel. For example, Fig. 1.1 shows 2D neutron radiographs of TRISO fuel kernels, revealing in one sample, voids/cavities. Neutron-based imaging has also been used in industrial radiography and for inspecting shielded shipping containers at border crossings, where strong metal shielding is likely to conceal illegal substances[44]. While photon cross sections show a strong atomic number dependence, neutron scattering cross sections are largely independent of atomic number. This results in neutron imaging having greater contrast in internal structures of high-Z materials, whereas X-rays or low-energy gamma rays experience too much attenuation to produce sufficient contrast for imaging [44–48]. That said, neutrons undergo considerable scattering in hydrogenous media such as water and plastics. The use of neutrons for imaging nuclear fuel underwater (e.g. a cooling pond) is complicated by the strong signal from randomly scattered neutrons, which blur the image.

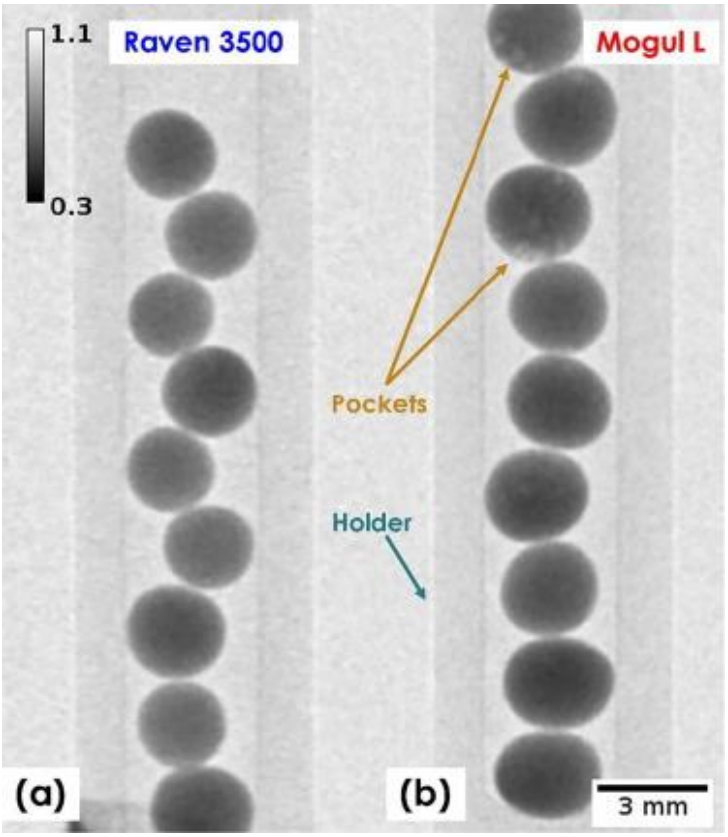

Figure 1.1. Normalized 2D neutron radiographs acquired for TRISO kernel spheres synthesized with (a) Raven 3500 carbon and (b) Mogul L carbon. [8]

1.1.2. X-Ray Imaging. Another common NDT approach for nuclear fuel examination is X-ray imaging. While it excels at studying low-density materials like soft tissues, plastics, and porous media, it struggles to give adequate contrast for dense materials like nuclear fuel. Because materials with similar mass densities exhibit little difference in contrast, X-ray imaging is mostly effective for studying cladding materials (usually medium-density alloys) that encase dense nuclear fuels [49–55]. Fig. 1.2 illustrates an X-ray imaging system including both transmission and rotation. The internal structure of the fuel, however, is usually obscured by the large attenuation and low contrast.

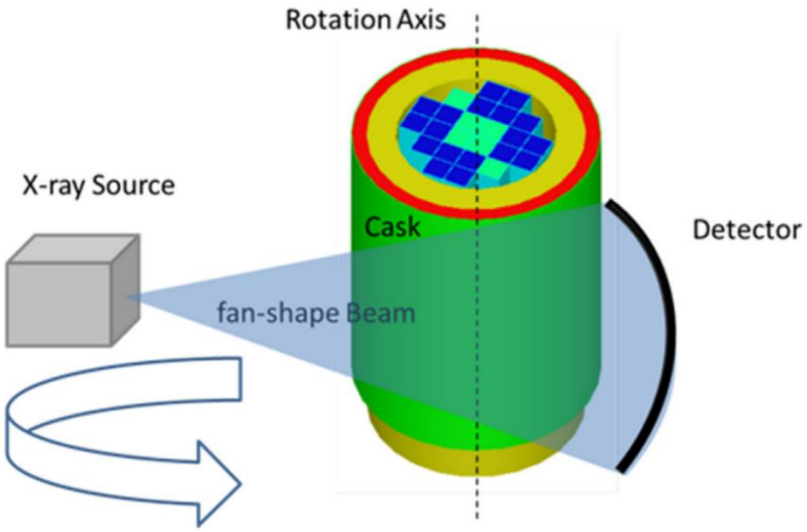

Figure 1.2. Drawing of an X-ray CT system. [56]

Phase Contrast Imaging (PCI) has been used to improve contrast at the interface between materials with similar mass densities [57–63]. PCI works by measuring the variations in refractive indexes between phase boundaries. This approach is most useful for analyzing TRISO particles with physical dimensions less than 1 mm in diameter. Fig. 1.3 shows the structure of a TRISO particle in good contrast using X-ray CT.

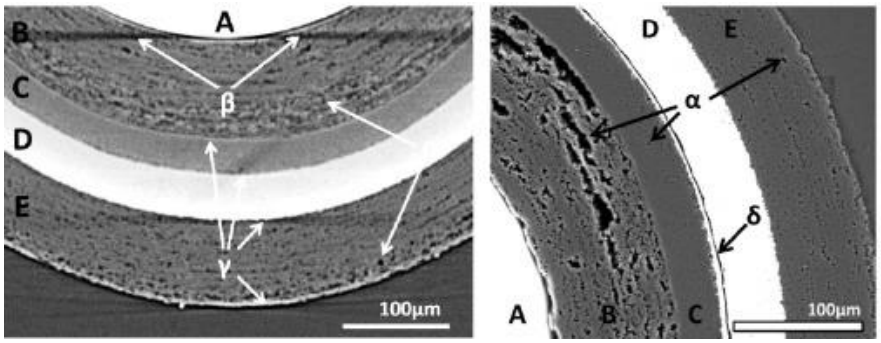

Figure 1.3. Magnified regions of interest of the TRISO particle using X-ray CT. [32]

1.1.3. Gamma Ray Imaging: Transmission and Emission. As with neutrons, gamma rays have high penetration power in dense media and are therefore useful in the non-destructive examination of actinide-containing materials such as nuclear fuel. Gamma-ray imaging is an effective method for detecting characteristic gamma radiation emitted by these isotopes and their decay products in the fuel [64]. Researchers have developed dedicated underwater measurement equipment for high background radiation [65, 66]. Gamma-ray imaging is also a widely established method used in several fields, such as medicine, astrophysics, and nuclear security. In the medical field, Gamma-ray imaging is employed to trace radioactive material injected, inhaled, or swallowed into the human body to observe the structure and function of organs or tissue. Although X-ray also can show images of the body, X-ray radiation passes through the body and the image shows the body parts in various shades of black and white because various tissues absorb radiation in different ways. Astrophysics utilizes gamma-ray imaging to detect high-energy cosmic photons and enable studies like observing astronomical objects and the evolution of stars. The detectors are deployed on balloons or spacecraft to avoid the radiation absorption of Earth's atmosphere [67]. Nuclear security denotes “the prevention and detection of, and response to, theft, sabotage, unauthorized access, illegal transfer or other malicious acts involving nuclear material, other radioactive substances or their associated facilities” [68]. Enriched ^{235}U or ^{239}Pu are of special importance due to the need for safeguarding and checking compliance with the Nuclear Non-Proliferation Treaty (NPT) [69]. The International Atomic Energy Agency (IAEA) has issued Guidelines for radioelement mapping using gamma-ray spectrometry data [70]. U.S. Customs and Border Protection (CBP) applies large-scale gamma-ray imaging systems to show the contents of cargo

containers and vehicles to detect and “prevent terrorists and terrorist weapons from entering the United States” [71]. Transmission gamma-ray computed tomography (CT) and Emission gamma-ray CT are two non-destructive imaging techniques that use gamma radiation to enable the assessment of structural integrity and the distribution of radioactive materials within an object.

1.1.3.1. Gamma-ray transmission CT. In transmission tomography, an external source transmits a signal through an object and measures it on the opposite side. This measured signal is then used to reconstruct information about the object's interior based on its gamma-ray attenuating properties [72]. Transmission CT measures the attenuation of gamma rays as they pass through an object, and the intensity of the transmitted gamma rays is measured by detectors placed on opposite sides of the object. Transmission CT is used to monitor the void fractions in the subchannels and to image the interior of nuclear reactors and fuel rods [73–86]. An example cone beam transmission CT system is shown in Fig. 1.4.

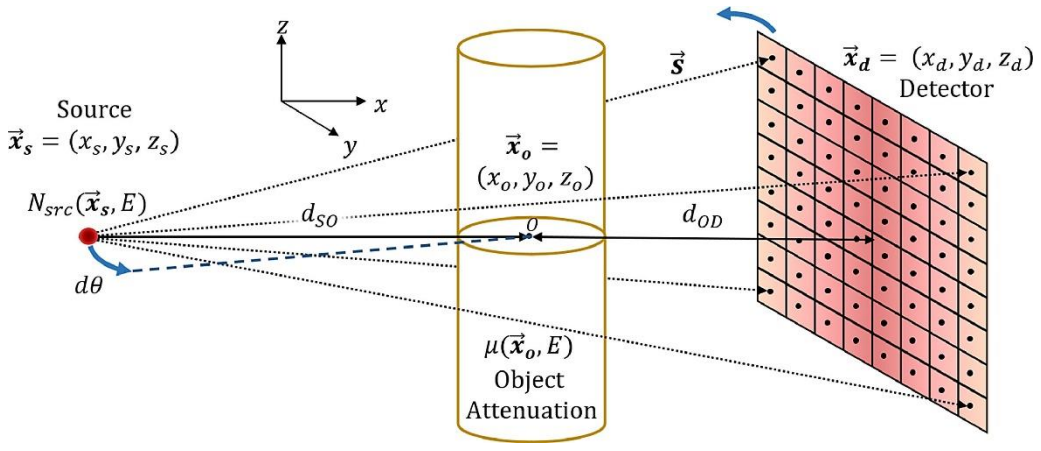

Figure 1.4. A cone beam transmission CT system. [50]

1.1.3.2. Gamma-ray emission CT. Emission tomography detects gamma rays emitted by radioactive material within an object and involves measuring a distributed source inside the object itself. A schematic diagram of an emission CT system is depicted in Fig. 1.5. This method is commonly used in the field of nuclear detection for imaging the distribution of radioactive materials in small objects, such as nuclear fuel pellets and sources, and for characterizing the properties of radioactive materials *in situ* [89–95]. Emission CT techniques include medical imaging techniques such as Single-Photon Emission Computed Tomography (SPECT) and Positron Emission Tomography (PET). SPECT uses radioactive material to evaluate blood flows in tissues and organs. It records gamma-ray emissions from the tissue or organ after administering a radiolabeled chemical into the body. PET uses isotopes emitting positrons that annihilate and produce two 511-keV gamma rays in opposite directions. By measuring the coincidences between these gamma rays using detectors, a 3D image can be reconstructed to map the positions of emitting gamma rays. Similar to medical imaging methods, spent nuclear fuel contains a variety of high-activity fission products that emit gamma rays through radioactive decay. These products can be detected using a gamma emission CT system.

Transmission CT and emission CT have notable differences [67]. If the gamma source is external to the fuel, the imaging system captures transmission data. However, in emission CT, the radiation sources are internal to the fuel, and the imaging system collects emission data. In transmission scans, the objective is to create an image that represents the map or distribution of attenuation coefficients within the fuel assembly. On the other hand, in emission scans, the desired image outcome is the distribution of decay products present within the fuel over time.

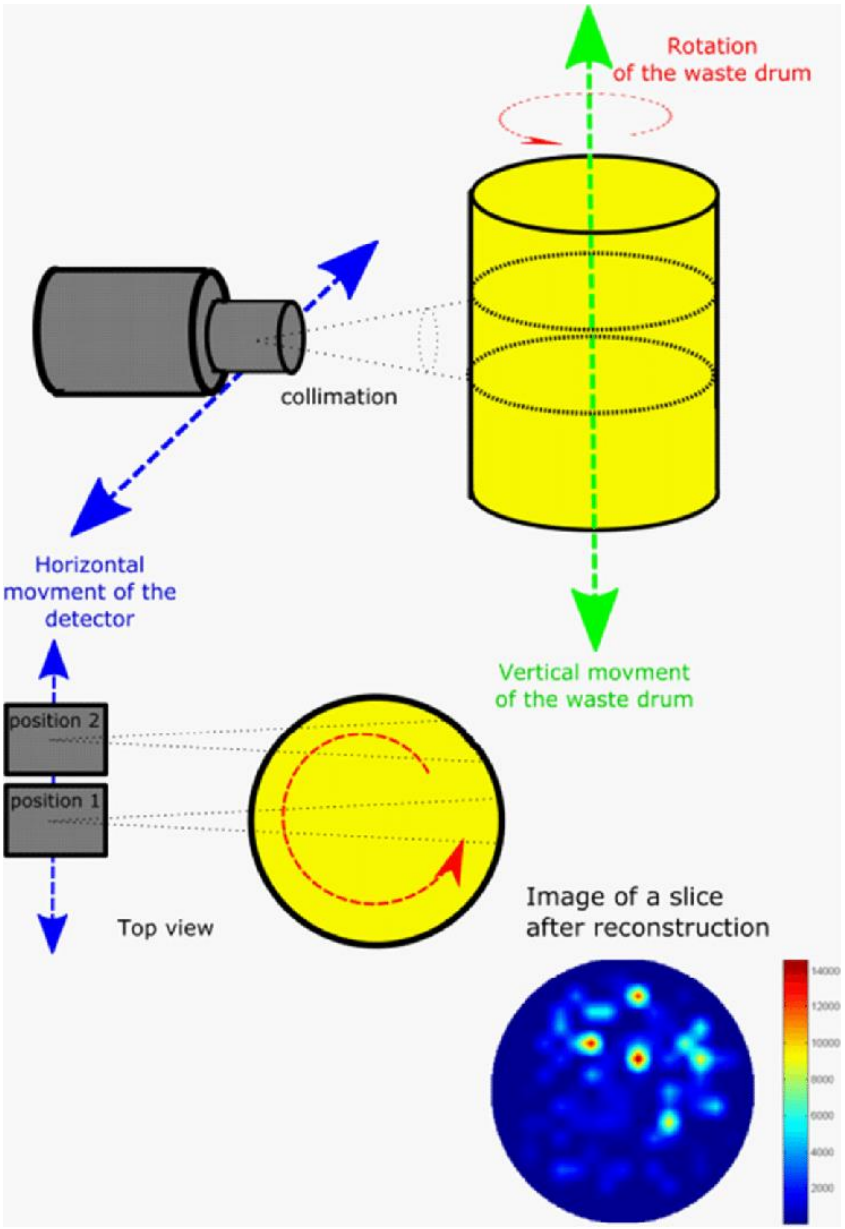

Figure 1.5. Drawing of an emission tomography characterization of radioactive waste at CEA, France. [96]

1.2. IMAGE QUALITY

Image quality refers to how accurately an image represents the object being imaged. It can be measured through the physical characteristics of the image or imaging system. Three important characteristics of nuclear images are spatial resolution (detail or

sharpness), contrast (difference in density or intensity between areas with different radioactivity concentrations), and noise (random fluctuations or structured noise from instrument artifacts). Spatial resolution, also known as resolving power, is a measure of how well an imaging system can reveal fine details, and the capacity to distinguish two adjacent structures as separate entities. In transmission X-ray or gamma-ray imaging, this is typically determined by using a test pattern made up of narrow lead strips and reported in terms of the number of line pairs per millimeter (lp/mm) that can be distinguished in the image. This can be seen in Fig. 1.6. Radiographic contrast refers to the degree to which different structures are distinguishable from one another in an image, based on their varying intensities in the image. This characteristic is illustrated in Fig. 1.7. This is influenced by factors such as the thickness, density, and chemical composition of the structures being imaged. In photon-based imaging techniques, primary photons are those that have not interacted with the structures in any way. On the other hand, scattered photons travel in fully or partially randomized directions. The image information is conveyed by primary photons; however, if any scattered photons reach the detector, they degrade the primary image and reduce its contrast.

These factors are interdependent, meaning that improving one may come at the expense of another. For example, better collimator resolution often leads to decreased efficiency, lower counting rates, and increased statistical noise.

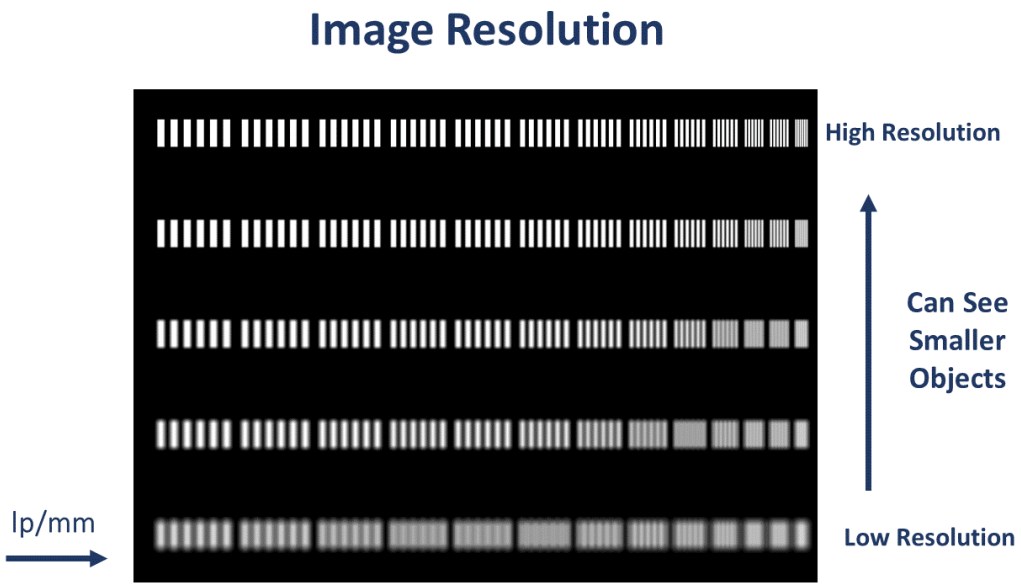

Figure 1.6. The resolving power of an X-ray imaging system is commonly measured through a test pattern. [97]

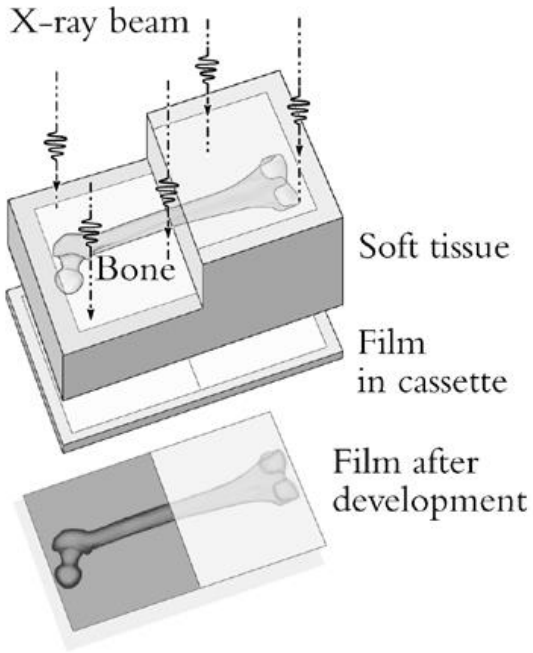

Figure 1.7. Radiographic contrast. [98]

1.2.1. Scintillation Detectors. Scintillators are materials, including solids, liquids, and gases that emit sparks or scintillations of light when ionizing radiation passes through them. However, the amount of light (number of visible or UV photons) produced in the scintillator per incident particle is typically below 100,000 and, therefore, requires amplification before it can be recorded as an electrical pulse or by other means. The operation of a scintillation detector involves two primary steps: first, absorption of incident radiation energy by the scintillator resulting in photon production within the visible part of the electromagnetic spectrum; secondly, amplification of this light via a photomultiplier tube or other sensitive light measurement device (e.g. avalanche photodiode) to produce an electrical output pulse. The diagram in Fig. 1.8 depicts a typical detection system using a scintillator. For this discussion, scintillators can be classified into three types: 1) Inorganic scintillators; 2) Organic scintillators; 3) Gaseous scintillators. [99]

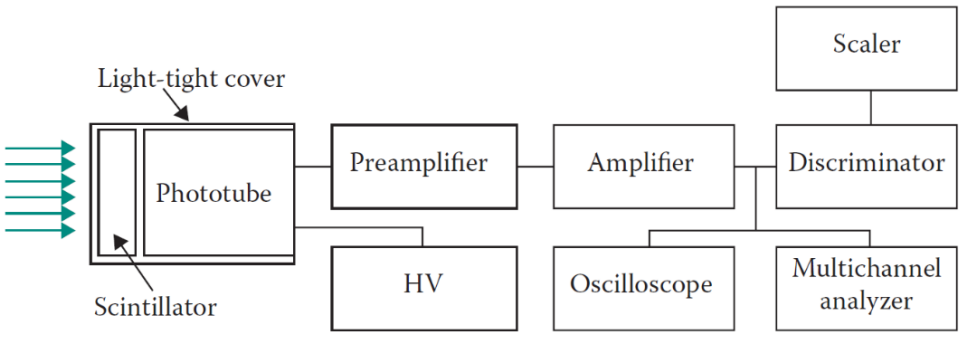

Figure 1.8. A detection system using a scintillator. [100]

1.2.1.1. Inorganic scintillators. Inorganic scintillators are primarily composed of crystals of halides, which have a low concentration of impurities. Some examples include NaI(Tl), CsI(Tl), CaI(Na), LiI(Eu), CaF_2(Eu) and $LaBr_3$(Ce) [99]. The element in

parentheses represents an activator species intentionally introduced into the crystal to enhance the luminescence efficiency.

Table 1.1. Properties of certain inorganic scintillators. [100]

Material	Wavelength of Maximum Emission (nm)	Scintillation Efficiency (Relative, %)	Decay Time (μs)	Density (10^3 kg/m^3)
NaI(Tl)	410	100	0.23	3.67
CaF_2(Eu)	435	50	0.94	3.18
CsI(Na)	420	80	0.63	4.51
CsI(Tl)	565	45	1.00	4.51
$Bi_4Ge_3O_{12}$	480	8	0.30	7.13
$CdWO_4$	530	20	0.90	7.90
^{6}LiI(Eu)	470	30	0.94	3.49

NaI(Tl) is a widely used scintillator for detecting gamma rays. It can be produced in single crystals up to 0.75 m in diameter and a considerable thickness of 0.25 m. Due to its high density (3.67 $\times$ 10^3 kg/m3), high atomic number, and large volume, it has very high efficiency as a gamma-ray detector [100]. Although semiconductor detectors have better energy resolution, they cannot replace NaI(Tl) when large detector volumes are required. The wavelength of maximum emission of NaI(Tl) is 410 nm, and the scintillation Efficiency is the highest among all the inorganic scintillators as shown in Table 1.1. However, NaI(Tl) has several undesirable properties as a material: it is brittle, hygroscopic, and sensitive to temperature gradients and thermal shocks. Therefore, it should always be

kept encapsulated [101]. Additionally, NaI always contains a small amount of potassium that creates background radiation due to radioactive decay from the presence of ^{40}K [102].

1.2.1.2. Organic scintillators. Organic scintillators are created by combining specific organic molecules and can be categorized as unitary, binary, ternary, etc., depending on the number of compounds in the mixture. One significant difference between inorganic and organic scintillators is their decay time: less than 10 ns for the latter (compared to ~1 μs for inorganic scintillators), making them suitable for fast timing measurements. The production of light in organic scintillators occurs due to molecular transitions.

Table 1.2. Properties of certain organic scintillators. [100]

Material	Wavelength of Maximum Emission (nm)	Relative Scintillation Efficiency (%)	Decay Time (ns)	Density (10^3 kg/m^3)
Anthracene	445	100	~30	1.25
trans-Stilbene	385	~60	4-8	1.16
NE 102	350–450	~65	2	1.06
NE 110	350–450	60	3	1.06
NE 213 (liquid)	350–450	~60	2	0.867
PILOT B	350–450	68	2	1.06
PILOT Y	350–450	64	~3	1.06

Organic crystal scintillators do not require an activator to enhance luminescence. Any impurities present in the crystal are undesirable because they reduce light output; therefore, materials used for crystal production must be purified.

Plastic scintillators are solid solutions of organic scintillators that can be shaped into various forms, from thin fibers to sheets. They are resistant to water, air, and many chemicals, making them suitable for direct contact with radioactive samples [103]. Additionally, they have a short decay time and emit light at wavelengths between 350 and 450 nm. Tin- and lead-loaded plastic scintillators have been tested as X-ray detectors in the 5-100 keV range. Thin plastic scintillator films, with a thickness of only 20 μg cm^{-2}, have been found to be effective detectors for time-of-flight measurements [99]. Table 1.2 shows a list of common organic scintillators and a comparison of their associated properties.

1.2.1.3. Gaseous scintillators. Gaseous scintillators are mixtures of noble gases that produce scintillations through atomic transitions. However, since the light emitted by noble gases is in the ultraviolet region, other gases like nitrogen are added to act as wavelength shifters [104]. Alternatively, thin layers of fluorescent materials can be used to coat the inner walls of the gas container for a similar effect. Gaseous scintillators possess several notable features: a very short decay time, light output per MeV deposited in the gas that depends little on the charge and mass of detected particles, and low efficiency for gamma detection [100]. These properties make gaseous scintillators ideal for measuring energy from heavy charged particles such as alphas, fission fragments, or other heavy ions but ill-suited for X-ray or gamma-ray imaging techniques.

1.2.2. Semiconductor Detectors. Semiconductor detectors operate similarly to ionization chambers but use charge carriers of electrons and "holes" instead of electrons and ions found in gas-filled detectors. The group IV semiconductors silicon and germanium have historically been the two most used materials in semiconductor detectors, although several compounds such as cadmium telluride (CdTe), cadmium zinc telluride (CdZnTe) or CZT, mercuric iodide (HgI_2), among others, have been developed [105]. The main advantage of semiconductor detectors over other radiation counters is their superior energy resolution allowing them to precisely determine and differentiate particle energies from a polyenergetic energy spectrum. The performance and operation of a semiconductor detector are influenced by various factors, including the type of material used (such as Si or Ge), as well as the manufacturing process, shaping, and treatment of the crystal. Therefore, characteristics such as size and shape also play a significant role in determining how well a semiconductor detector functions. At room temperature, electrons in Si and Ge have enough thermal energy to move into the conduction band and create thermal noise [106]. This can degrade detector resolution. To prevent this, operating the detector at lower temperatures (usually at or below liquid nitrogen temperature) is necessary for high-energy-resolution gamma-ray spectroscopy. Reducing the physical size of a semiconductor detector can also enhance its performance at room temperature by reducing the number of electrons it contains, resulting in less thermal noise. This approach, while not suitable for gamma spectroscopy due to the unacceptable loss of efficiency, is used in a surface barrier and Passivated Implanted Planar (PIP) Si detectors for charged particle spectroscopy. The wider bandgaps of CdTe, CZT, and HgI_2 result in far lower concentrations of thermally

generated carriers at room temperatures. Such semiconductors have shown to be useful for room-temperature gamma-ray spectroscopy.

1.3. SUBMERSIBLE GAMMA-RAY COMPUTED TOMOGRAPHY SYSTEM

The Fuel Imaging and Examination by Submersible Tomography Analysis (FIESTA) system is a gamma-ray tomography instrument intended to be set up in the canal of the Advanced Test Reactor at Idaho National Laboratory [107]. Fig. 1.9 showcases the components and principle of image formation of the FIESTA system. This submersible system will be used to inspect irradiated fuel capsules using gamma-ray-tomography. The proposed design aims to image the internal structure of the fuel as a function of burnup through gamma-ray transmission computed tomography. Additionally, it will use gamma-ray emission computed tomography to map out the distribution of fission products by detecting their characteristic gamma-ray emissions.

During transmission CT mode, a focused beam of gamma rays originating from a Co-60 source is directed toward the fuel specimen. The specimen undergoes both translation and rotation while in the path of the beam. Variations in the intensity of the beam detected at a NaI detector are recorded as a function of changes in the orientation of the specimen, which are then utilized to create an accurate 3D structural image. On the other hand, during emission CT mode, specific gamma radiation emissions from fission products present within active fuel samples are identified using pixelated CdZnTe (CZT) detectors and pinhole apertures. A series of energy-filtered emission radiographs are captured to generate images that depict distributions of fission products.

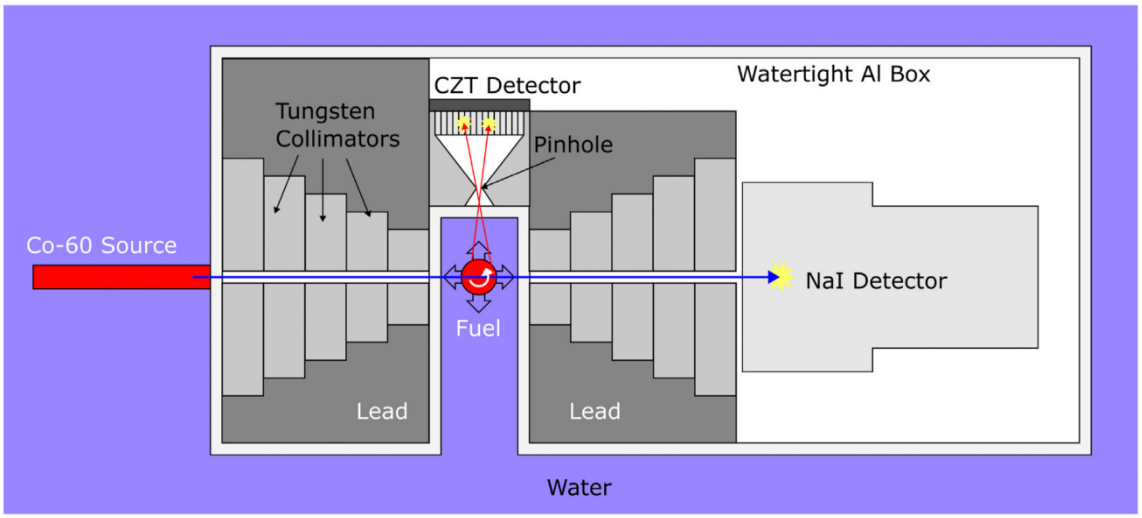

Figure 1.9. Diagram (not to scale) showing FIESTA system components and image generation principle. [108]

1.3.1. System Design. Fig. 1.10 depicts a Computer-Aided Design (CAD) model of the FIESTA system. The FIESTA system is meant to sit on a working tray, which is a movable submerged platform mounted to the canal wall (Figure 1.10a). In transmission CT mode, a high activity (>1 kCi) ^{60}Co source rod is placed in a V-grooved source holder and can be removed for emission tomography measurements. The transmission and emission radiographs are taken using a pair of lead and tungsten collimators. A pair of pencil-beam collimators define a narrow ^{60}Co transmitted beam, which is measured by a NaI scintillator detector, as illustrated in the quarter section view of Figure 1.10(b). In the quarter section view, just one of the pencil-beam collimators can be observed. A pixelated CdZnTe (CZT) detector captures spatial and spectral information using a pinhole collimator oriented 90 degrees to the transmission axis. To keep detectors and shielding elements safe from canal water, they are housed in a watertight box. The fuel rodlet can be positioned in the middle of the collimators while maintaining contact with the canal water

thanks to a notch in the box. A sample manipulator, as shown in Figures 1.10(c) and (d), is used to sample radiographic projections. The rodlet is gripped and rotated by the sample manipulator using a three-jaw chuck mounted to a rotary stage driven by a precision stepper motor. Meanwhile, the stage is translated horizontally and vertically through the pencil beam by three high-precision linear actuators.

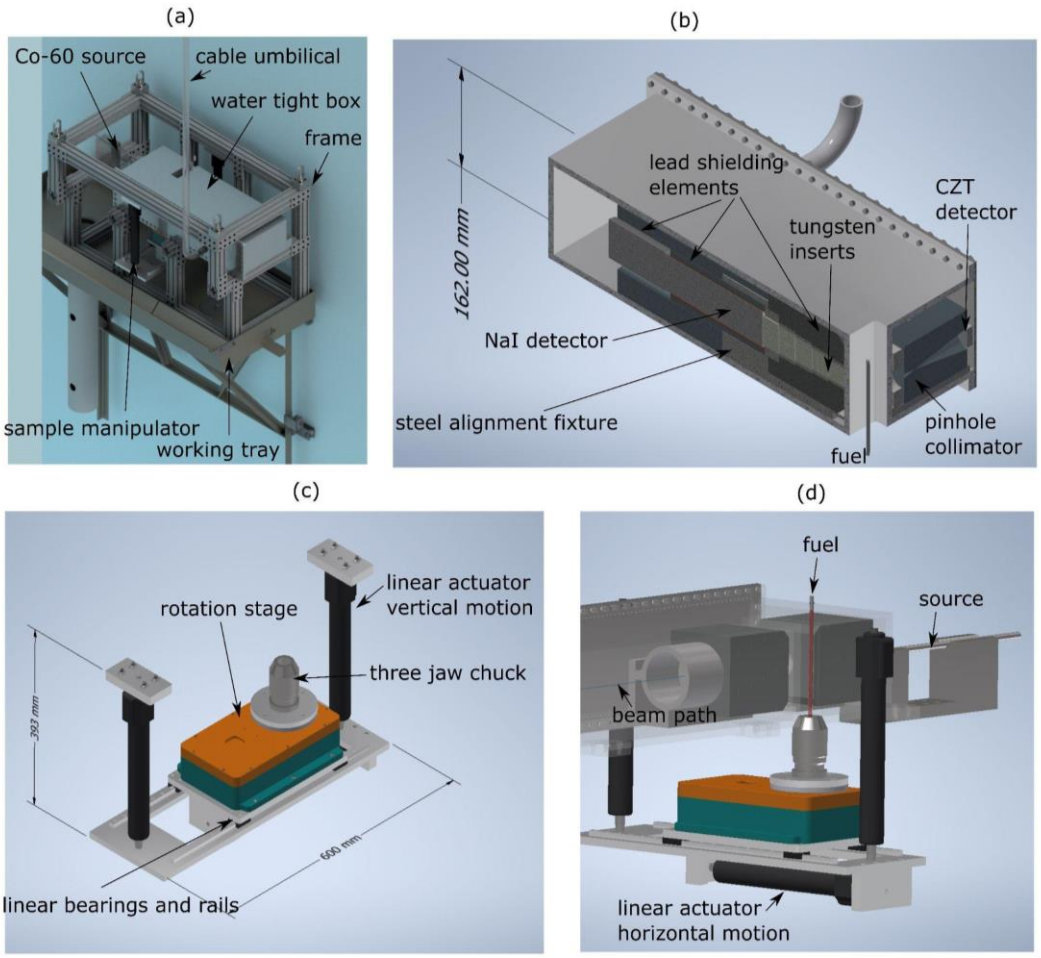

Figure 1.10. The FIESTA system includes a) an illustration of its installation at the ATR canal, b) a 1/4 section view of the watertight box displaying inner collimator assemblies and detectors, c) a sample manipulator consisting of a rotation stage and linear actuators, and d) a side view of the sample manipulator that translates fuel capsule through transmission beam (NaI detector and shielding elements are not shown).[108]

1.3.2. Collimator Design. A parallel beam collimator is an essential component in many nuclear detection systems, as it allows for selective detection of ionizing radiation in a specific direction while reducing the background noise and improving the sensitivity of the system[17, 109]. The collimator is typically made of dense material, such as lead or tungsten, and is designed to absorb radiation that is not traveling in the desired direction, thus improving the signal-to-noise ratio of the detector. FIESTA requires a high-aspect tungsten collimator with an aperture of 200 μm and a length of at least 15.5 cm. The parallel beam collimator design is shown in Fig. 1.11. To fabricate such a collimator with the required precision and tolerance, several cylindrical tungsten segments are used, each with an angularly offset slot and concentric hole. These segments are inserted into a high-tolerance CNC machined steel alignment fixture and machined using wire Electrical Discharge Machining (EDM). To reduce the possibility of photon streaming through gaps in the collimator, each consecutive tungsten segment has an increasing diameter in a step-like arrangement, and each section is rotated to ensure that no two wire-entry-slots overlap.

A pinhole collimator is a type of collimator used particularly in single-photon emission computed tomography (SPECT) and gamma-ray imaging applications. The pinhole collimator consists of a small aperture or pinhole, typically made of lead or tungsten, that allows only a narrow beam of gamma rays to pass through in a straight line. Fig. 1.12 provides a visual representation of a pinhole collimator. The design of a pinhole collimator involves several important considerations, including the diameter and length of the pinhole, the distance between the pinhole and the detector, and the material and thickness of the collimator [110, 111]. The diameter of the pinhole determines the resolution of the system, with smaller pinholes providing higher resolution but lower

sensitivity. The length of the pinhole affects the collimation efficiency and the amount of scatter and background radiation that reaches the detector. The distance between the pinhole and the detector, also known as the focal length, is another critical parameter that affects the resolution and sensitivity of the system. Lead and tungsten are commonly used materials for pinhole collimators, with thicker collimators providing higher attenuation and better collimation efficiency.

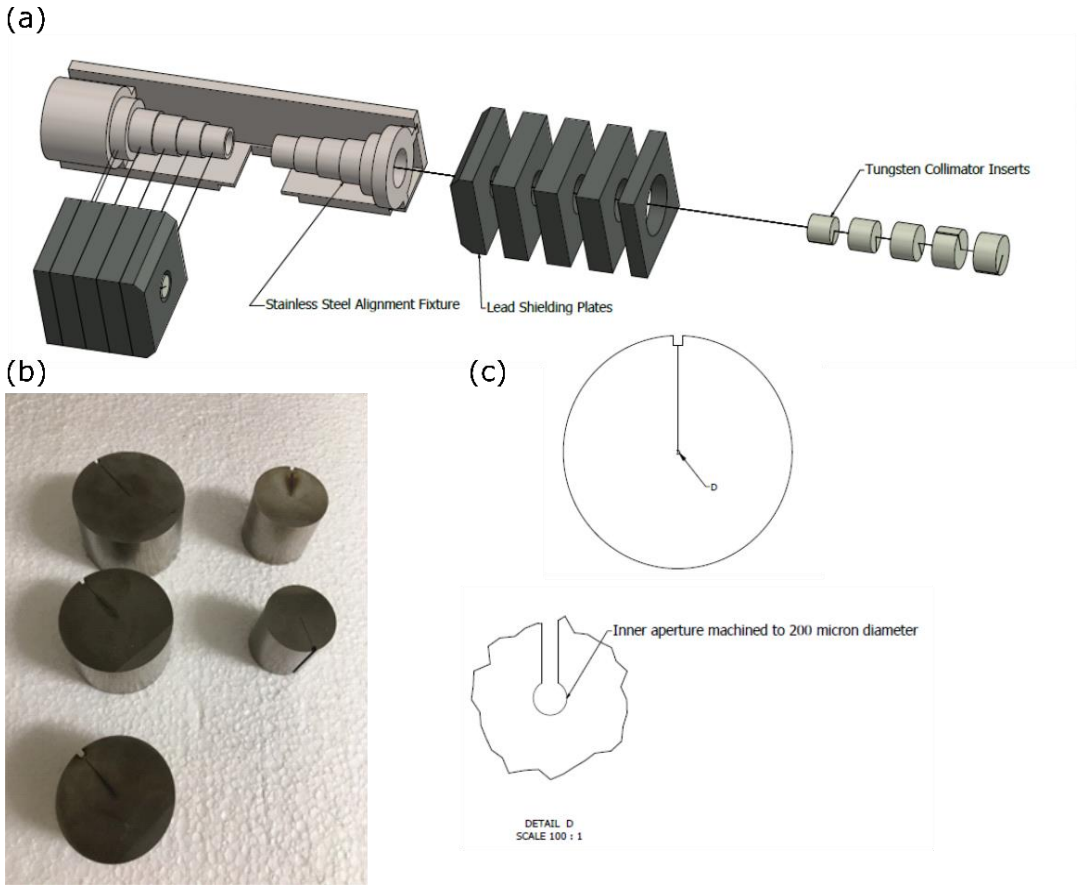

Figure 1.11. Pencil-beam collimator design. a) assembly of a pencil-beam collimator b) Tungsten sections with varying diameters made through wire-EDM c) Drawing illustrating the cuts made in tungsten section using wire EDM. The inner diameter in detail D is 200 μm. [108]

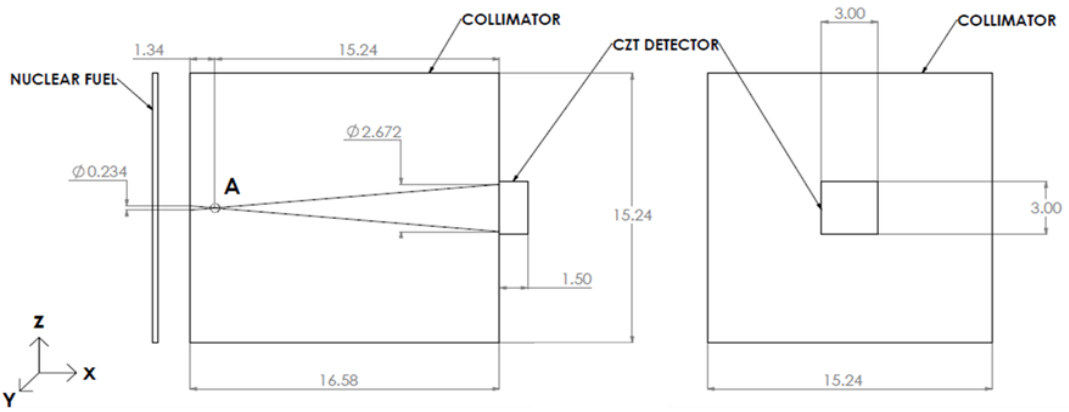

Figure 1.12. Pinhole collimator design combined with a CZT detector. [108]

1.4. MODELING

The Monte Carlo model was created using the simulation tool Monte Carlo N-Particle (MCNP6) [112]. The MCNP model is shown in Fig. 1.13. MCNP is a versatile and widely used general-purpose Monte Carlo radiation transport code that simulates the behavior of particles, such as neutrons, photons, and electrons, in complex geometries. MCNP can provide highly accurate simulations of particle behavior, which takes into account the complex interactions that occur between particles and materials. The code has been extensively validated against experimental data, providing confidence in its ability to accurately model radiation transport problems. MCNP includes many advanced features, such as variance reduction techniques and parallel processing, which allow for efficient and accurate simulations. However, MCNP's material libraries are limited in scope, which can make it difficult to accurately model certain materials, and the code may not be suitable for modeling other types of particle behavior or physical phenomena [113–115]. The Monte Carlo method is a statistical simulation technique that samples several particle histories during radiation transit. It can precisely define the geometries and material properties of a system, as well as track primary and secondary radiations and all essential

interactions during the transport process. This method, when combined with reliable data libraries and models, is undoubtedly the most physically realistic numerical methodology for modeling radiation detection systems [116].

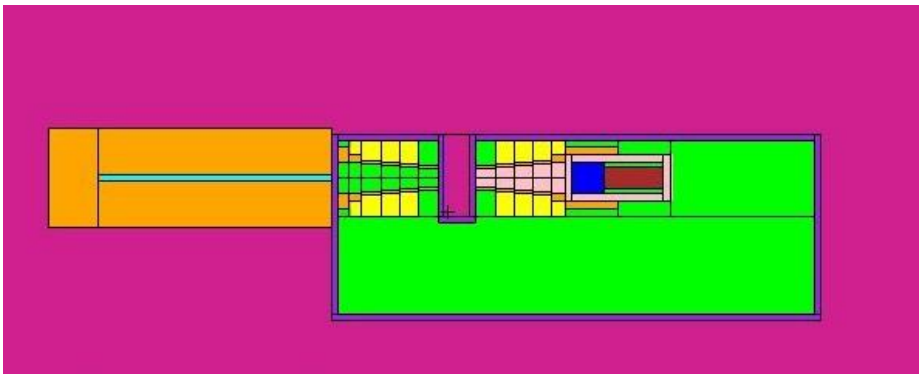

Figure 1.13. A well-shielded FIESTA model.

PAPER

I. ACCELERATED RADIATION TRANSPORT MODELING TECHNIQUES FOR PENCIL BEAM COMPUTED TOMOGRAPHY USING GAMMA RAYS

Zhongmin Jin[1], Seth Kilby[1], Ashish Avachat[1], Bryant Kanies[1], Nicolas Woolstenhulme[2], Hyoung K. Lee[1], Joseph Graham[1]

[1]Missouri University of Science and Technology 301 W 14th St. Rolla, MO 65409

[2]Idaho National Laboratory 1955 N. Fremont Avenue Idaho Falls, ID 83415

ABSTRACT

Monte Carlo radiation transport modeling studies were performed for a compact, and high-resolution gamma-ray computed tomography system designed for imaging irradiated nuclear fuel. The system comprises a ^{60}Co source - chosen for its highly penetrating 1173 keV and 1332 keV gamma rays - a pair of high-aspect-ratio pencil beam collimators, and an inorganic scintillator detector. Two acceleration methods are proposed to rapidly model a transmission type gamma-ray tomography system. The first, a variance reduction technique, is based on performing Monte Carlo simulations with a monodirectionally-biased source, sampled from a characteristic sub-volume of the full source volume. The second acceleration method is based on the deterministic calculations using the Beer-Lambert law and detector response characteristics. Comparison of simulations using acceleration approaches with analog simulations of the fully isotropic, full-volume equivalent, show that the Monte Carlo variance reduction technique gives quantitatively accurate predictions for large collimator aspect ratios while the deterministic

calculations are semi-quantitative but converge close to the correct result as the collimator aspect ratio increases. As such, these techniques can be used to reduce the computational cost in generating simulated radiographs and tomographs by several orders of magnitude. Experimental validation efforts are currently underway and will be demonstrated in future work.

Keywords: Radiation transport, non-destructive testing, gamma-ray tomography, Monte Carlo, nuclear fuel

1. INTRODUCTION

Poolside non-destructive test (NDT) methods allow researchers to measure physical properties of irradiated nuclear fuel in a rapid way without needing to remove the high activity fuel from cooling ponds where they are left to decay after irradiation. This method offers researchers the ability to characterize new fuel and materials at different snapshots of burnup or irradiation dose. In-pile irradiation experiments are essential for qualifying materials for eventual adoption in advanced reactor designs and the nuclear fuel cycle. NDT methods that aid in characterizing the qualitative and quantitative structural changes occurring in nuclear fuels under irradiation are sought [1-3]. Past studies have used tomographic methods to simulate and experimentally investigate fuel assemblies [4-6]. A proposed submersible gamma-ray computed tomography (CT) system is being designed to eventually perform pool-side fuel characterization of individual test fuel rodlets at the Advanced Test Reactor (ATR) at Idaho National Laboratories (INL) [7]. The purpose of the proposed system is to perform structural characterization of irradiated fuel rodlets from

ATR using transmission CT. With transmission CT, the obtained image is constructed from a set of radiographic projections acquired by translating and rotating the object through the gamma ray beam. Using image reconstruction algorithms, a 3-dimensional distribution of the mass attenuation coefficients of the fuel rodlet is obtained. For gamma rays with energies near 1 MeV, mass attenuation coefficients are approximately proportional to mass density, Compton scattering being the dominant interaction around 1 MeV for most substances. Such information can be used to visualize changes in the 3D density image of fuel (i.e. structural evolution) as a function of burnup. Structural changes such as volumetric swelling, cracking, relocation, and restructuring are important as they affect fuel performance related parameters such as heat transfer coefficients, centerline temperature, and fission gas release rates. Modeling radiation transport of the transmission CT module is the focus of this work.

The analog Monte Carlo radiation transport method is arguably the most physically accurate numerical approach in modeling radiation detection systems [8]. In analog Monte Carlo techniques, transport of a particle follows all of the relevant interaction physics expected in the real-world problem. This method has been widely used in CT simulations and validated by experiments. However, in some Monte Carlo problems, particle losses that occur due to absorption and scattering can vastly outnumber the particle histories of interest, such as those that contribute to a certain tally. Indeed, in the detection system considered here, high-spatial-resolution images are acquired utilizing a pair of high-aspect-ratio (ratio of collimator thickness to aperture diameter), pencil beam collimators 200 microns in diameter with lengths of about 15 cm. For such a high aspect ratio, the solid angle subtended by the aperture opening on the detector is small and the vast majority of

photons emitted from the source are unlikely to contribute to the tally (count rate) of interest. Therefore, analog Monte Carlo transport is computationally demanding and inefficient.

For CT problems, computational costs are further compounded as simulations must be repeated over many projections to reliably reconstruct a three-dimensional image. To alleviate some of the computational burdens without sacrificing the quality of images, researchers have presented approaches with improved computing resources (e.g., upgraded hardware and software), alternative deterministic methods [9-13], as well as combining adaptation methods with the Monte Carlo method [14-16]. These methods mainly pertain to radiotherapy calculations and may not be directly transferable to the specific geometries and interactions of importance to specialized CT systems.

Because of the inherent inefficiency of analog transport in systems with high-aspect-ratio collimators and the need for many projections in a CT reconstruction, direct analog simulation is not viable. The goal of this work is to accelerate the simulation of transmission CT radiographs while preserving the essential physics of particle transport and detection. Monte Carlo radiation transport modeling studies were performed for a compact and high-spatial-resolution gamma-ray computed tomography system designed for imaging irradiated nuclear fuel.

Two acceleration methods are proposed to aid in the simulation of projection radiographs. The first, a variance reduction technique, is based on performing non-analog Monte Carlo simulations with a monodirectionally-biased source while the second is based on deterministic calculations using the Beer-Lambert law combined with detector response factors calculated using separate analog Monte Carlo simulations. These methods of

modeling the gamma-ray transmission problem were benchmarked for different collimator diameters to evaluate the range of validity of their assumptions.

2. METHODOLOGY

2.1. DESCRIPTION OF THE MODEL

The calculations for this work are based on a submersible 3D imaging system designed for performing pool-side fuel characterization. The layout of the transmission imaging system comprises the following major components: a multi-kCi strength ^{60}Co gamma source, a source collimator, the object being examined (a small nuclear fuel rodlet approximately 15 cm in height), a detector collimator, and a $LaBr_3(Ce)$ detector [17].

The Monte Carlo model was developed in the Monte Carlo N-Particle (MCNP6) simulation package [7]. MCNP is a general-purpose Monte Carlo radiation transport code. Fig. 1 shows the cell geometries in the Monte Carlo model of the transmission system. A ^{60}Co source emits gamma rays at 1.173 MeV and 1.332 MeV, which are ideal for probing high-Z elements owing to the near-minimum mass attenuation coefficients for most elements at those energies. Dense objects, such as the nuclear fuel rodlets considered here, are most transparent at the minimum mass attenuation coefficient. Transparency is desirable for achieving higher contrast in the thickest part of the fuel. In comparison, X-rays can only penetrate the lower mass thickness cladding and cannot provide any structural information about the fuel inside. The ^{60}Co source was defined as a cylindrical volume of cobalt metal in a shielded lead container. The isotropic source was 1 cm in diameter and 38.1 cm long, with an activity of 2.56×10^{15} Bq. Collimation was achieved using a pair of

lead collimators of thickness 15 cm each. A parallel cylindrical collimator opening was placed in the center. The aperture size, the diameter of the cylindrical opening of the collimator, was treated as an independent variable. The water gap between the two collimators was 6.28 cm. This source was first collimated to provide a pencil beam (parallel beam) of photons for radiographic projections. The pencil beam then passes through the center of the imaging object, a fuel rodlet containing uranium dioxide fuel, before being re-collimated by a second collimator. The density of the 4.5% enriched uranium dioxide (UO_2) fuel rod was 10.5 g cm^{-3}. The diameter of the fuel rod was 0.478 cm, which was based on those of the actual radiation test specimens at ATR. The final beam is analyzed by an inorganic scintillator detector. The size of the cylindrical scintillator crystal was set to 5.08 cm in diameter and 5.08 cm in height, large enough in volume to contain most of the Compton cascade regions within it. The source was assumed to be a solid piece of cobalt metal. In MCNP simulations, attenuation was implicitly included through the photon transport. A pulse-height tally (F8) was used to determine the spectral response of the detector. A surface flux tally (F2) at the source-facing surface of the scintillator crystal was also used to determine the intensity of incident gamma rays through the collimator and into the detector [8].

This actual system is designed to have a 200-micron diameter collimator aperture, and an isotropic source placed 37.28 cm away from the detector. Because of such designs, the probability of a source photon interacting with the detector is extremely low, owing to the geometric attenuation of the uncollided photons. The majority of photons are absorbed by one of the two collimators during radiation transport. To simulate the gamma-ray spectrum and count rate using a full-volume and isotropic source definition (analog

transport) with reasonable statistics and computation time, the aperture diameter had to be increased to at least 5 mm. Even then, variance reduction cards (e.g., IMP card) were used to 1) terminate the particle's history when it enters the collimator, 2) control the particle population entering a specific element of the system through geometry splitting and Russian roulette, and 3) scale the cutoffs in the weight control game. Statistical convergence can be improved efficiently with these techniques [8, 18].

2.2. DETERMINISTIC CALCULATIONS

2.2.1. Intensity of Uncollided Photons. Uncollided photons are photons that have streamed directly from the source to the detector without any collisions or interactions in-between. As discussed in the introduction, deterministic methods have the benefit of being rapid, albeit with variable accuracy. In the simplest treatment, the transport of photons from the source to the detector was modeled as a 1D attenuation problem. The uncollided photon flux at the detector was estimated using the Beer-Lambert law [19] considering simple exponential attenuation, tabulated energy-dependent mass attenuation coefficients, μ(E)/ρ, of the materials [20], and their theoretical densities, ρ:

$$I(E,x) = I_0(E)e^{-\frac{\mu(E)}{\rho}\rho x} = I_0(E)e^{-\mu(E)x} \quad (1)$$

$I(E,x)$ is the intensity of the transmitted radiation beam with photon energy E, $I_0(E)$ is the intensity of the incident beam, $\mu(E)$ is the linear attenuation coefficient of the material, and x is the linear thickness of the material. At the energies of ^{60}Co gamma rays, 1.173 MeV and 1.332 MeV, $\mu(E)$ has a relatively weak contribution from photoelectric absorption, and as such, pair production, and Compton scattering dominate.

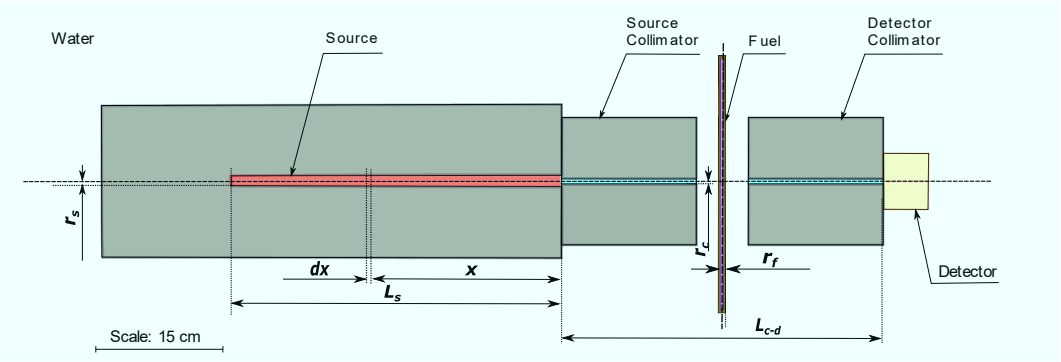

Figure 1. Basic MCNP model of the tomography system with a cylindrical ^{60}Co source. The model consists of: a shielded cylindrical ^{60}Co source, a source collimator, a fuel rodlet, a detector collimator, and a $LaBr_3$(Ce) detector.

The ^{60}Co source emits photons isotropically at a rate of 2.56×10^{15} s^{-1}. Eq. 1 assumes gamma rays travel monodirectionally in straight lines. Therefore, the initial intensity used in the Beer-Lambert Law should be adjusted for the solid angle of the detector. A solid angle correction factor is derived with a point source approximation in Eq. 2.

$$f_{\Omega}(x) = \frac{\text{area of collimator aperture}}{\text{area of sphere at detector}} = \frac{\pi r_c^2}{4\pi(L_{c-d}+x)^2} \tag{2}$$

r_c is the radius of the collimator aperture, $L_{c\text{-}d}$ is the total end-to-end length of both collimators, and x is the distance between the source particle's sampled location and the collimator. This equation assumes a 1D distribution of isotropically emitted source particles along the beam axis. As only a fraction of the source volume is within the field-of-view of the detector, a sub-volume correction factor is given by

$$f_{\text{v}} = \frac{\pi r_c^2 L_s}{\pi r_s^2 L_s} = \frac{r_c^2}{r_s^2} \tag{3}$$

where r_s is the radius of the cylindrical source, and L_s is the length of the source. This equation accounts for the large fraction of the source occluded by the collimators. It holds

approximately if the collimator aspect ratio (the collimator length-to-diameter ratio) is significantly greater than unity. In truth, the solid angle depends on the differential volume element, so Eqs. 2 and 3 cannot truly be uncoupled but must instead appear as terms in a 3D integral over the cylindrical source volume. These factors can thus be viewed as approximations. Additionally, the sub-volume correction factor is not applicable when the radius of the source is smaller than the collimator aperture. To account for self-absorption effects in the source, the linear attenuation coefficient of cobalt was used. Applying these correction factors to the Beer-Lambert law and integrating over the ^{60}Co source distribution, the intensity of uncollided photons which have passed through the center of the fuel rodlet and reached the scintillator is given by

$$I = A_0 f_{\mathrm{v}} \int_0^{L_s} f_\Omega(x) \exp\left[-\left(\mu_s x + 2\mu_f r_f + 2\mu_w L_w\right)\right] dx \tag{4}$$

where A_0 is the activity of the source and μ_s is the linear attenuation coefficient of the source. In other words, the intensity of photons incident on the detector face is equal to the activity from each differential slice (thickness dx) within the source from the start of the source collimator ($x = 0$) to the end of the source ($x = L_s$), and corrected for field of view effects (f_{v}) and solid angle effects $f_\Omega(x)$. μ_f, and μ_w are the linear attenutation coefficients of fuel and water, respectively; r_f is the radius of the cylindrical fuel; and L_w is the beam path length through the water. Combining Eqs. (2-4) gives

$$I = \frac{A_0 r_c^4}{4 L_s r_s^2} \int_0^{L_s} \frac{\exp\left[-(\mu_s x + 2\mu_f r_f + 2\mu_w L_w)\right]}{(L_{c-d} + x)^2} dx \tag{5}$$

The uncollided photon intensities were calculated using Eq. 5 in Matlab will be compared with Monte Carlo simulations in the results section.

2.2.2. Detector Response Function. There are three dominant types of photon interactions that contribute to the total absorption in the detector. These interactions include the photoelectric effect, Compton scattering, and pair production [17]. The quantity that gives the fraction of particles counted per unit time relative to the total number that interacts within the detector volume is called the detector efficiency ε and is defined as follows [19]

$$\varepsilon = \frac{\text{number of particles recorded per unit time}}{\text{number of particles impinging upon the detector per unit time}} \quad (6)$$

The full-energy peak efficiency is given by [19]

$$\text{Full energy peak efficiency} = \text{detector efficiency} \times \frac{\text{counts in full-energy peak}}{\text{total counts in spectrum}} \quad (7)$$

The peak-to-total ratio (P) is the proportion of counts in a full-energy photopeak to the total counts in a spectrum. As discussed in introduction, the full-energy peak efficiency of the $LaBr_3$(Ce) detector can be predicted with analog MCNP simulations. However, lower energy scattered photons can reach the detector from other sources such as the water and fuel. This skews the peak-to-total ratio and detector efficiency. To mitigate this, the detector response factors were calculated using an idealized MCNP model. The $LaBr_3$(Ce) detector was put in a vacuum surrounded by a graveyard (area where particle histories are killed) and facing a disk source emitting gamma particles monodirectionally. This model ensures that only the interaction and transport physics of the detector contribute to the detector response factors. The size of the disk source corresponds to the collimator aperture size in the other MCNP models.

Thus, the photopeak count rate can be predicted for a given flux of incident photons by multiplying the intensity of uncollided photons in Eq. 5 by the full-energy peak efficiency in Eq. 7, provided the incident flux of scattered photons into the detector solid

angle is negligible. In other words, numerical or analytical predictions of the uncollided flux of sufficiently monoenergetic photons into the detector can be straightforwardly multiplied by a normalized detector spectral response to yield a qualitatively and quantitatively accurate gamma-ray spectrum. The validity of the monoenergetic assumption will be discussed.

2.3. MONODIRECTIONAL BIASING

An accelerated Monte Carlo transport method was explored, which uses directional source biasing. This monodirectional biasing was introduced by modifying the full-volume, isotropic source definition card (SDEF) with two additional entries

VEC=0 1 0 DIR=1

which convert the isotropic source into a monodirectional source with all photons initially traveling towards the detector along the collimator axis. The VEC and DIR cards were used to assign the initial direction of source particle flight [8]. DIR card specifies the cosine of the angle between the initial direction of the particle and the reference vector VEC, which is parallel to the collimator axis. DIR=1 gave a monodirectional source in the direction of VEC.

The basic idea behind this approach is simple. Photons outside of the detector field of view, which would almost assuredly be absorbed in the collimator or transported away from the detector, were all ignored. Essentially, mass attenuation and scattering, assuming these occur, are forced to occur near the collimator axis or within the scintillator crystal. The resulting signal, therefore, accounts for absorption and scattering losses from the uncollided flux as well as detector response (e.g., Compton scattering in the scintillator)

while spending far less computational effort on photons that have virtually zero probability of reaching the detector. In contrast to a purely analytical calculation, this approach still models the detector response. An analytical prediction of the detector response is a highly non-trivial problem as it must necessarily include 3D radiation transport, multiple scattering, and continuous photon spectra. Therefore, the Monte Carlo method is better suited to the detector response portion of the problem. The directional biasing approach is useful in this highly collimated system as it significantly increases the efficiency of the Monte Carlo simulations compared with the fully isotropic analog cases. However, because the approach greatly overestimates the per-source-particle detector count rate, an analytical correction factor to convert monodirectional counts to the equivalent isotropic counts should be introduced to estimate the unbiased results. The monodirectional correction factor f_{mono} accounts for a fraction of photons emitted towards the detector to the total number of photons isotropically emitted from the source. Also, attenuation physics in the cobalt source must be taken into consideration. This factor is defined as follows,

$$f_{mono} = \frac{\int_0^{L_S} \frac{\pi {r_c}^2}{4\pi(L_{c-d}+x)^2} \exp(-\mu_s x) dx}{\int_0^{L_S} \exp(-\mu_s x) dx} \tag{8}$$

Eqs. 8 is similar to Eq. 5 apart from the mass attenuation terms in the fuel and water and the sub-volume terms. The sub-volume normalization is accounted for in the MCNP source definition while mass attenuation and scattering in the water and fuel are implicitly calculated in the simulation. It is interesting to quantitatively compare the results of a fully analog Monte Carlo transport calculation and monodirectionally biased calculations to a

simple analytical calculation. A MATLAB script was written to evaluate Eq. 5 to benchmark the Beer-Lambert approximation with the Monte Carlo calculations.

3. RESULTS, DISCUSSION, AND OUTLOOK

Fig. 2 shows the gamma-ray spectra generated by pulse height tallies (F8) from the isotropic source simulations in MCNP. The chosen aperture diameters were 1.0 cm, 1.5 cm, and 2.0 cm. Each spectrum was normalized to the photopeak counts at 1.332 MeV. To achieve less than 5% statistical uncertainty in the Monte Carlo simulations, 10^9 particle histories were tracked. The computational time needed for the simulations was between 1,744-1,820 min, depending on aperture size, on an Ubuntu Linux system running on a virtual machine with 4 GB of memory. The virtual machine runs on an HP Z400 workstation in a Windows 10 system. The physical workstation has a 3.2 GHz 4-core, 8-thread Intel Xeon W3565 processor with 8 GB of RAM. It can be seen from Fig. 2 that the peak-to-total ratios for different collimator sizes are in good agreement with each other, showing that the spectral shape is already converged for apertures below 2.0 cm. The similarity of spectral shapes (and of peak-to-total ratios) shows that the detector response is uncoupled from the scattering that is occurring in any other part of the system. It is the Compton scattering in the scintillator crystal that mostly dominates the Compton background for collimators with large aspect ratios (15 or higher). This partially justifies using a monodirectionally biased source in place of an isotropic source as Compton scattering in the source, fuel, and water does not significantly contribute to the detector response. The high aspect ratio collimator is effective in rejecting collided photons.

Moreover, fully analog Monte Carlo simulations for such a small collimator become increasingly computationally expensive as the collimator size decreases.

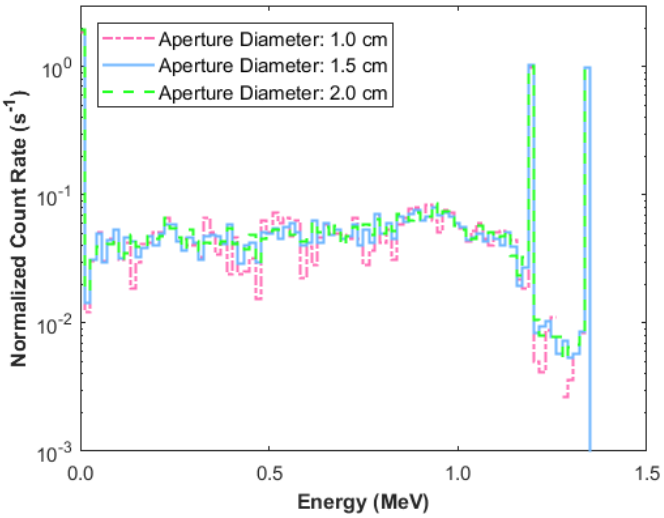

Figure 2. Idealized ^{60}Co spectrum with different aperture diameters (normalized to photopeak counts; no broadening effects).

As mentioned previously, the cylindrical source extends a comparatively long distance (38.1 cm) along the beam axis. It is, therefore, necessary to consider the attenuation within the source as well. Fig. 3 shows the spectra gained with different source materials from MCNP simulations with an isotropic source distribution. As shown in Fig. 3a, the count rate is reduced by nearly a factor of ten when switched from air to ^{60}Co. To ensure the reliability of the deterministic results, the source was discretized along its length, and the mass attenuation coefficient of the source was taken into consideration. Fig. 3b shows that the detector peak-to-total ratio is mostly insensitive to the choice of sources.

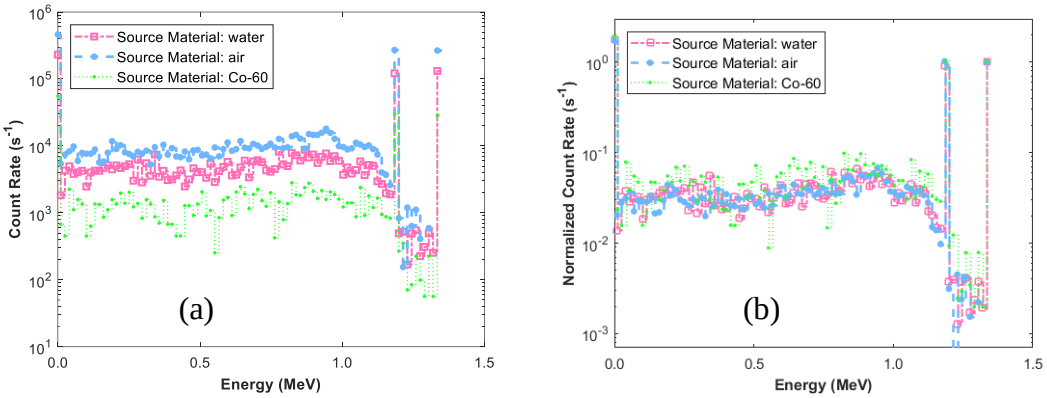

Figure 3. Gamma-ray spectra in different source materials with a 1 cm aperture (a) absolute count rate (b) count rate normalized to peak counts at 1.332 MeV.

In the remainder of this paper, all results and discussion of source intensities and photopeak counts will pertain to the 1.332 MeV photopeak. The results at 1.332 MeV are unaffected by photons scattered from higher energies, which permits a more lucid analysis of the results. However, both gamma rays at 1.173 MeV and 1.332 MeV showed similar results. Two more sets of aperture diameters (0.5 cm, and 3.0 cm) are taken into consideration to show the trend. Besides relative error, figure of merit (FOM) is another measurement of the effectiveness of a certain method in reducing the variance of the results. This is defined as

$$FOM = \frac{1}{R^2 T} \tag{9}$$

where T is the simulation time, and R is the relative error. FOM is also reported in the standard MCNP output file. To achieve uncertainties less than 1%, MCNP simulations took 290 min of computer time for the monodirectional source and produced a FOM of 3.00×10^{3}. To achieve the same uncertainties 12,440 min of computer time is required for the isotropic source using a 1.5 cm collimator aperture and produced a FOM of 1.12×10^{0}.

Smaller apertures increase this time considerably for the isotropic cases but not for the monodirectional cases.

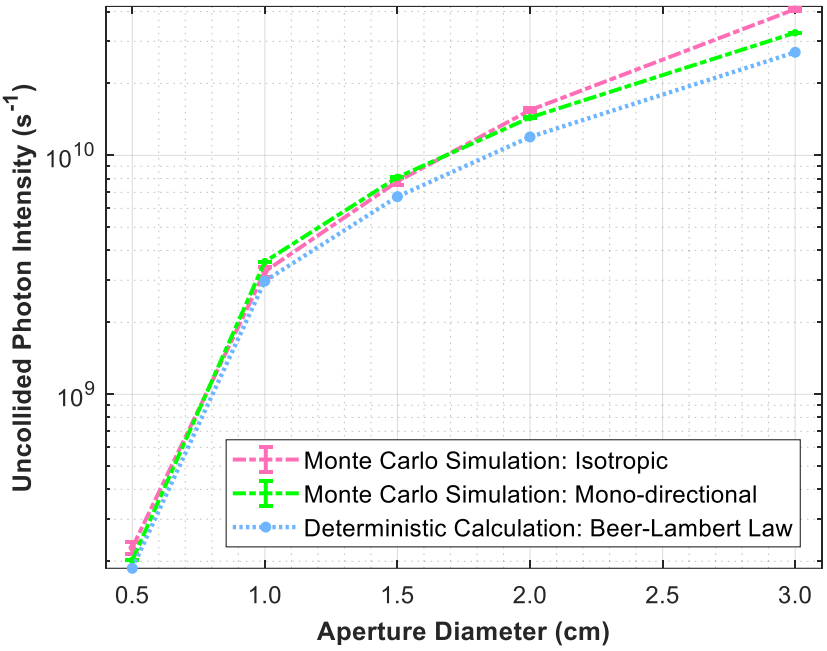

Figure 4. Uncollided photon intensity comparison of fully analog and monodirectional transport with analytical calculations at 1.332 MeV.

Fig. 4 shows the uncollided incident gamma-ray intensities calculated by the isotropic transport, Beer-Lambert law, and monodirectional transport methods with corresponding analytical correction factors. As expected, the flux of uncollided photons decreases with decreasing aperture size. It can also be seen that both the Beer-Lambert Law approximation and monodirectional biasing simulations converge rapidly to the analog Monte Carlo results with decreasing aperture size. The monodirectional biasing technique shows better agreement (average percent error of -4%) with the fully analog simulations than does the Beer-Lambert law (average percent error of -20%). This is not surprising as

the Beer-Lambert law is a 1-dimensional model and may exclude certain effects, e.g. small angle scattering. Furthermore, the mass attenuation coefficient characterizes how easily electromagnetic radiation penetrates a material, and the choice of its database plays an essential role in the accuracy of the results. MCNP uses the continuous-energy photon ACE format data, which is a compact version of the Evaluated Nuclear Data File format [21]. Attenuation data for Beer-Lambert Law calculations were based on the National Institute of Standards and Technology XCOM database of attenuation coefficients [20]. Even small differences between the MCNP and Beer-Lambert Law results could be due to the mass attenuation coefficients that are from different data libraries or simply by uncertainties introduced by the Monte Carlo method. Also, the source sub-volume within the field-of-view of the detector is more accurately described by a truncated cone rather than a narrow cylinder, especially for apertures with small aspect ratios. More simply put, Eq. 5 tends to underestimate the number of source photons that reach the detector. The correction factor of the monodirectional calculations accounts for five orders of magnitude difference in source emission solid angle from the analog case, the complexity of the attenuation in the source cannot be ignored. It is performing the source integrals numerically that increases the accuracy. In the case of problems involving isotropic source emission and thick collimators, small solid angle losses can significantly reduce the ratio of tallied particles to total particle histories. Recasting the problem into one with an equivalent geometry and source strength can vastly reduce the variance and improve computational efficiency.

The detector response factors for 1.332 MeV photons (peak-to-total ratio and detector efficiency) are shown in Fig. 5. For aperture diameters smaller than 0.5 cm, a peak-to-total ratio between 41.5%-42% can be assumed.

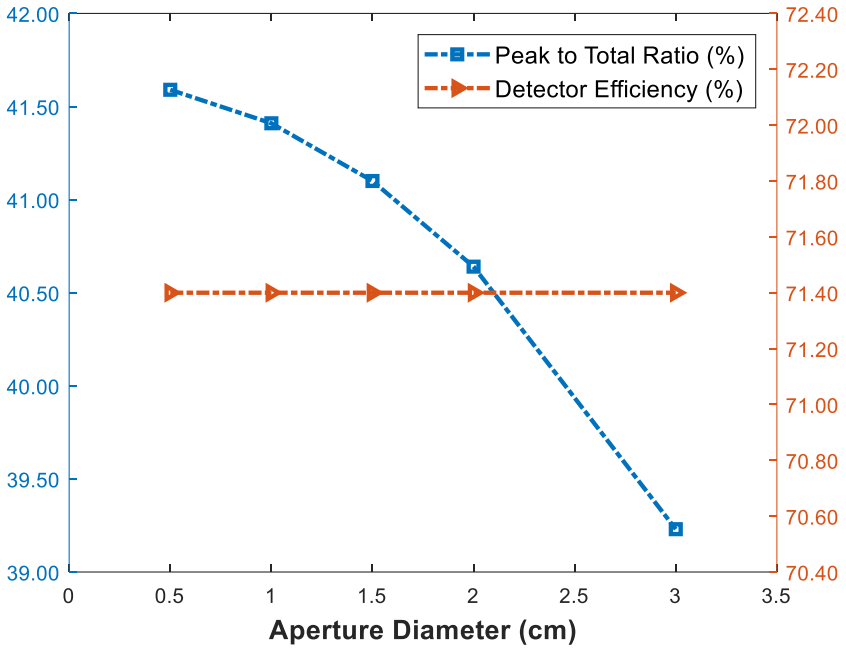

Figure 5. Detector response factors vs. aperture size.

In Table 1, the relationships among isotropic photopeak counts (C_{ISO}) Beer-Lambert law photopeak counts (C_{BL}), and monodirectional photopeak counts (C_{MONO}) are similar to those in Fig. 4. The larger discrepancy from the Beer-Lambert law calculation may either reflect the aforementioned limitations of that essentially 1D model or else reflect the limitations of assuming that the detector response is uncoupled from transport in the source, fuel, and collimator.

Table 1. Comparison of photopeak counts in the detector (1.332 MeV). Figures of merit are given for each simulation.

Aperture diameter (cm)	Ratio		FOM	
	C_{MONO} / C_{ISO}	C_{BL} / C_{ISO}	ISO	MONO
0.5	0.920 ± 0.062	0.851 ± 0.062	2.16×10^{-2}	9.84×10^{2}
1.0	1.066 ± 0.035	0.885 ± 0.035	4.47×10^{-1}	3.02×10^{3}
1.5	1.002 ± 0.022	0.824 ± 0.022	1.12×10^{0}	3.00×10^{3}
2.0	0.947 ± 0.015	0.768 ± 0.016	2.14×10^{0}	3.02×10^{3}
3.0	0.864 ± 0.004	0.677 ± 0.004	4.83×10^{0}	2.91×10^{3}

These results indicate that the monodirectional MCNP method is efficient in that it either saves a significant amount of computational time or, given a computational time, produces a higher FOM, when compared to analog simulations assuming an isotropic source. It gives a qualitatively correct spectral shape and can quantitatively predict the detector response factors accurately as the contribution of Compton scattering occurring outside of the detector is small, as can be seen by the overlapping spectra in Fig. 2 (differences in the magnitude of the Compton continuum are within statistical fluctuations). Quantitatively, the Beer-Lambert Law calculations of the uncollided photon intensity are comparable to the results of isotropic simulations differing by less than 20% for the 1 cm diameter aperture. That said, the Beer-Lambert Law calculations are still less accurate that the monodirectionally biased Monte Carlo simulations. Perhaps most importantly, the accuracy of both the Beer-Lambert calculation and the monodirectional simulations improve with decreasing aperture sizes. It is at small apertures where the analog Monte

Carlo method suffers the greatest computational inefficiencies and where both of these accelerated methods become advantageous.

Regardless of the source of the remaining discrepancies, the photon intensities of the MCNP simulations remain proportional to the deterministic calculations. This suggests that it is reasonable to calculate a spectrum that is both qualitatively and quantitatively predictive by first normalizing the monodirectional spectrum to the intensity of gamma rays at 1.332 MeV, then multiplying the normalized spectrum by the calculated intensity of gamma rays at 1.332 MeV using the Beer-Lambert law method and, finally, adjusting the error to reflect realistic counting statistics. The counting statistics of the pulse-height tally (Fig. 6) in each channel follows Poisson statistics [22]. The relative error is given by

$$R_i = \frac{1}{\sqrt{C_i}} \tag{10}$$

R_i is the relative error in channel i; C_i is the counts in channel i. To generate hundreds of radiographic projections needed to reconstruct a 3D image, this method could be used to efficiently simulate the transmission of the Co-60 gamma rays through different chords within the fuel representing translations and rotations in the imaging system. By doing so, simulated multi-channel spectra are generated which resemble the actual spectra collected by the experimental apparatus that will be used in the construction of sinograms and 3D images.

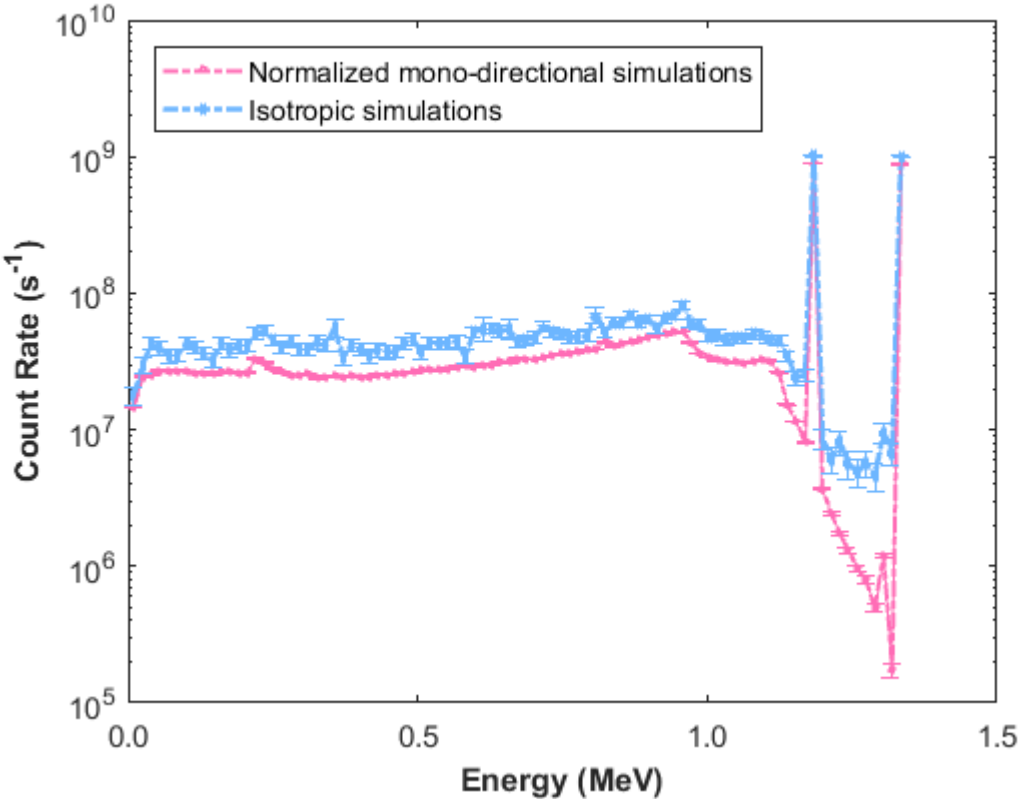

Figure 6. Spectra obtained by: scaling a normalized spectrum determined from simulation with monodirectional source by the Beer-Lambert uncollided photon intensity (bottom curve) and from analog simulation with isotropic source (top curve). The aperture size is 1.0 cm.

4. CONCLUSIONS

A Monte Carlo model of a submersible 3D imaging system for performing gamma-ray computed tomography was developed and used to simulate transmission gamma-ray spectra in a scintillator detector. Comparisons were made between fully analog MCNP simulations with an isotropic source, MCNP simulations with a monodirectionally biased source combined with a solid angle correction factor, as well as deterministic calculations based on the Beer-Lambert law. The results show that the monodirectional MCNP

simulations qualitatively and quantitatively agree with the analog results for large collimator aspect ratios, while the deterministic calculations are accurate enough (within ~15% error) for semi-quantitative predictions of the uncollided photon intensity.

A significant gain in computational efficiency is seen with the monodirectionally biased Monte Carlo method with a typical simulation generating data with orders of magnitude higher figure of merit and completing in less time. Meanwhile, it only takes the deterministic method seconds to generate the uncollided photon intensity and multiply it by the detector response factors. In either case, these techniques offer the modeler the ability to simulate entire projection radiographs, and even full 3D tomographs. The same cannot be said for the fully analog technique. Though somewhat slower than the deterministic method, monodirectional biasing accounts for more of the correct interaction physics than the Beer-Lambert law. However, the Beer-Lambert law, when combined with a method for incorporating the detector response and statistical noise, may also allow modelers to produce simulated radiographs in a very short time. Though these techniques may be limited to specific class of collimator and detector geometries, it may be possible to use them to perform rapid simulations of 3D tomographs on a desktop computer. The current work focuses on acceleration techniques and benchmarking computational methods rather than validation. Such validation efforts are currently underway and will be demonstrated in future work.

ACKNOWLEDGEMENTS

This work was supported by the U.S. Department of Energy, Nuclear Energy University Programs, project 17-13011.

COMPLIANCE WITH ETHICAL STANDARDS

The authors declare that they have no conflict of interest

REFERENCES

1. J. Schulthess, N. Woolstenhulme, A. Craft, J. Kane et al, Non-Destructive post-irradiation examination results of the first modern fueled experiments in TREAT, Journal of Nuclear Materials, 541 (2020) 152442.

2. S. Lorenzo, V. Rathore, A. Anastasiadis, E.A. Sundén et al, Evaluation of gamma-ray transmission through rectangular collimator slits for application in nuclear fuel spectrometry, Nuclear Instruments and Methods in Physics Research Section A: Accelerators, Spectrometers, Detectors and Associated Equipment 1014 (2021) 165698.

3. R. Cesareo, A. Brunetti, R.T. Lopes, G. Galli, D.V. Rao, A. Castellano, G.E. Gigante et al, X-and gamma-ray tomography for nondestructive material testing, in: Proc. SPIE's International Symposium on Optical Science, Engineering, and Instrumentation, Denver, CO, United States, 1999.

4. S. Jacobsson, A. Håkansson, P. Jansson, A. Bäcklin. A tomographic method for verification of the integrity of spent nuclear fuel assemblies—II: experimental investigation, Nuclear technology, 135 (2001) 146-153.

5. S. Jacobsson, C. Andersson, A. Håkansson, A. Bäcklin, A tomographic method for verification of the integrity of spent nuclear fuel assemblies-I: Simulation studies, Nuclear Technology, 135 (2001) 131-145.

6. S. Holcombe, S.J. Svärd, L. Hallstadius, A Novel gamma emission tomography instrument for enhanced fuel characterization capabilities within the OECD Halden Reactor Project, Annals of nuclear energy, 85 (2015) 837-845.

7. C.J. Stanley, F.M. Marshall, Advanced Test Reactor: A National Scientific User Facility, in: Proc. 16th International Conference on Nuclear Engineering, Orlando, FL, United States, 2008.

8. T. Goorley, M. James, T. Booth, F. Brown, J. Bull, L.J. Cox, J. Durkee et al, Initial MCNP6 release overview, Nuclear technology, 180 (2012) 298-315.

9. K.A. Gifford, J.L. Horton Jr, T.A. Wareing, G. Failla, F. Mourtada, Comparison of a finite-element multigroup discrete-ordinates code with Monte Carlo for radiotherapy calculations, Physics in Medicine & Biology, 51 (2006) 2253.

10. J.C. Wagner, D.E. Peplow, S.W. Mosher, T.M. Evans, Review of hybrid (deterministic/Monte Carlo) radiation transport methods, codes, and applications at Oak Ridge National Laboratory, Progress in nuclear science and technology, 2 (2011) 808-814.

11. Y. Kyriakou, T. Riedel, W.A. Kalender, Combining deterministic and Monte Carlo calculations for fast estimation of scatter intensities in CT, Physics in Medicine & Biology, 51 (2006) 4567.

12. C. Börgers, Complexity of Monte Carlo and deterministic dose-calculation methods, Physics in Medicine & Biology, 43 (1998) 517.

13. A. Bingham, H.K. Lee, The viability of ADVANTG deterministic method for synthetic radiography generation, Computer Physics Communications, 228 (2018) 5-10.

14. H. Lee, C. Yoon, S. Cho, S.H. Park, W. Lee, The adaptation method in the Monte Carlo simulation for computed tomography, Nuclear Engineering and Technology, 47 (2015) 472-478.

15. D. Sarrut, L. Guigues, Region-oriented CT image representation for reducing computing time of Monte Carlo simulations, Medical physics, 35 (2008) 1452-1463.

16. D.E. Peplow, K. Verghese, Digital mammography image simulation using Monte Carlo, Medical physics, 27 (2000) 568-579.

17. F. Quarati, A.J.J Bos, S. Brandenburg, C. Dathy et al, X-ray and gamma-ray response of a 2 ″ × 2 ″ LaBr3: Ce scintillation detector, Nuclear Instruments and Methods in Physics Research Section A: Accelerators, Spectrometers, Detectors and Associated Equipment, 574 (2007) 115-120.

18. C.R. Harrell, I.G. Zubal, Effect of variance reduction techniques on Monte Carlo simulated energy spectra, in Proc. IEEE Seventeenth Annual Northeast Bioengineering Conference, Hartford, CT, United States, 1991.

19. N. Tsoulfanidis, Measurement and Detection of Radiation, 2nd ed., CRC press, Boca Raton, 1995.

20. M. J. Berger, J.H. Hubbell, S.M. Seltzer, J. Chang, J.S. Coursey, R. Sukumar, D.S. Zucker, K. Olsen, XCOM: photon cross section database, v1.5, 2010. https://dx.doi.org/10.18434/T48G6X

21. M.B. Chadwick, P. Obložinský, M. Herman, N.M. Greene, R.D. McKnight, D.L. Smith, P.G. Young et al, ENDF/B-VII. 0: next generation evaluated nuclear data library for nuclear science and technology, Nuclear data sheets, 107 (2006) 2931-3060.

22. A.D. Barbour, L. Holst, S. Janson, Poisson approximation, The Clarendon Press Oxford University Press, New York, 1992.

II. USE OF A FAST PLASTIC SCINTILLATOR TO DETECT LOW INTENSITY GAMMA RAYS IN AN INTENSE, LOW ENERGY BACKGROUND

Zhongmin Jin[1], Seth Kilby[1], Ashish Avachat[3], Nicolas Woolstenhulme[2], Hyoung K. Lee[4], Joseph Graham[1]

[1]Missouri University of Science and Technology 301 W 14th St. Rolla, MO 65409

[2]Idaho National Laboratory 1955 N. Fremont Avenue Idaho Falls, ID 83415

[3]University of Pittsburgh, 3700 O'Hara St, Pittsburgh, PA 15261

[4]University of New Mexico, Albuquerque, NM 87131

ABSTRACT

A measurement technique using a fast plastic scintillator and pulse-height discrimination was investigated to improve the sensitivity of detecting low intensity, high-energy gamma rays from a high intensity, lower-energy gamma-ray background. A low activity ^{60}Co source was used as a high-energy signal and ^{137}Cs sources were used to emulate high-intensity, lower-energy backgrounds. Count rates were measured as a function of discrimination threshold for three different flux ratios of ^{60}Co/^{137}Cs. It is demonstrated that by optimizing the low-level discriminator voltage, it was possible to reduce the count time required to limit of quantification (LOQ) by several orders of magnitude. The applicability of this technique in scenarios where a high activity source is present in a strongly scattering medium is discussed.

Keywords: Radiation measurement, non-destructive testing, gamma-ray discrimination, high activity counting, plastic scintillator

1. INTRODUCTION

Quantitative determination of the activities and characteristic emission peaks of high energy (>1 MeV), high intensity gamma-ray sources immersed in a scattering medium (liquid or solid) is made more challenging by the contribution of scattered photons. If the distance between source and detector is on the order of several mean free paths for Compton scattering, a large majority of the detected photons will be low energy scattered photons (see Fig. 1). Such situations are found in, for example, nuclear research and test reactors—where pool-side experiments and apparatus are being developed to characterize the irradiated fuel elements by using gamma radiation from high activity ^{60}Co sources as an imaging probe. The activities of such sources tend to range from tens to thousands of Ci [1–3]. To shield the sources and provide adequate natural convective cooling, operations are conducted underwater, either in the reactor pool or an adjacent storage canal [4–7]. The scattering properties of water must therefore be considered in design of such radiation measurement experiments.

Given a sufficiently low activity source, energy windowing or energy spectroscopy can be used to isolate the incident uncollided counts from the incident background of low-energy scattered photons [8–10]. This can be done, for example, using a standard inorganic scintillator detector, such as NaI(Tl), or a semiconductor detector, such as high purity Ge detector (HPGe).

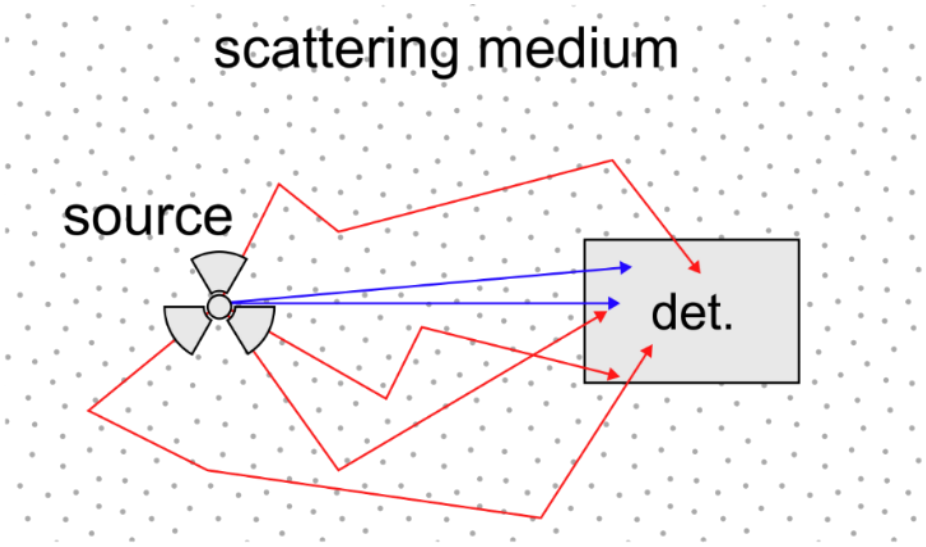

Figure 1. Measurement of the activity of a gamma emitter in a strong scattering medium involves discriminating counts from higher-energy uncollided photons (blue) from lower-energy scattered photons (red). When the source-to-detector distance is multiple scattering mean free paths, the scattered contribution can dominate the total count rate.

If the source has a high activity, time resolution becomes an important factor. Both inorganic scintillators and semiconductor detectors have relatively long tail pulse rise times. For example, NaI has a characteristic decay time of ~240 ns and HPGe detectors typically operate with a charge collection time on the order of 100 ns per cm of collection depth [11]. Thus, shaped pulses are typically no narrower than ~1 μs if energy spectroscopy is to be performed [12]. When the source has tens to thousands of Ci of activity and is placed in a strong scattering medium, such as water, the interaction rate from low energy scattered photons may be on the order of ~10 MHz or greater. At such interaction rates, the deadtime approaches 100% for shaped pulses typical of inorganic scintillators and semiconductor detectors. Such overwhelming deadtimes make the inorganic scintillator and semiconductor detectors unsuitable for applications where a high activity source is

placed in a scattering medium, especially without any additional shielding to reduce the contribution from the scattered photons [13–17].

Distance and shielding are effective strategies at combating deadtime issues encountered with energy sensitive but slow detectors. In applications where distance and shielding cannot be exploited for combating the said deadtime issues, detectors with fast timing characteristics can be used. Fast plastic scintillators have pulse widths on the order of nanoseconds [12]. Such detectors can extend interaction rates up to ~100 MHz before significant deadtime losses are incurred [12]. That said, plastic scintillators are rarely used for spectroscopy as they offer poor energy resolution when compared to inorganic scintillators and semiconductor detectors [18–20]. When there is an extensive overlap between the low-energy scattered photons and high-energy, uncollided photons in the pulse-height spectrum, the ability to accurately quantify the activity of the source is lost. Thus, there is a need for a viable plastic scintillator-based strategy for quantifying the flux of uncollided photons from a high activity source placed in a highly scattering medium.

In this work, we report such a strategy using an economic nuclear instrumentation that is easily available in a laboratory setting—single channel analyzer (SCA). Specifically, the pulse height discriminator of the SCA was used to separate the signal counts of ^{60}Co with low activity and higher emission energies from the background counts of ^{137}Cs with a high activity and low emission energy.

2. METHODOLOGY

2.1. EXPERIMENTAL SETUP

Counts from the sources, ^{60}Co (1.17 MeV and 1.33 MeV) and ^{137}Cs (0.662 MeV), were alternately acquired using a fast plastic scintillator detector from Alpha Spectra Inc. The scintillator plastic (ASI-100) has a polyvinyl toluene polymer base, 2.5 ns pulse width, and density of 1.02 g cm^{-3} [21]. The ^{137}Cs was used to emulate lower-energy scattered photons from a scattering medium, instead of placing the ^{60}Co source in a scattering medium such as water. The actual experiments were conducted in air for convenience. The spectrum of scattered ^{60}Co photons is expected to be continuous and will depend on the scattering medium and source-to-detector distance. For the purposes of this experiment, however, it was only important that the background source contains lower photon energies at higher intensities/fluxes. The ^{60}Co source from our setup was a low activity check source that had an activity of 0.0573 μCi at the time of the experiment. A 38.5 mCi ^{137}Cs source was used to emulate a strong background (relative to the ^{60}Co source) of lower-energy photons. The distance between the ^{137}Cs source and the detector was used to vary the flux ratio of ^{60}Co and ^{137}Cs photons.

The pulse processing setup consists of a constant fraction discriminator (Ortec model 583B) with an approximately 10 ns pulse width and a counter (Canberra 2071A) (see Figure 2). Negative NIM logic pulses were used. The pulse pair resolution of the system is limited by the discriminator which is specified to be 50 ns.

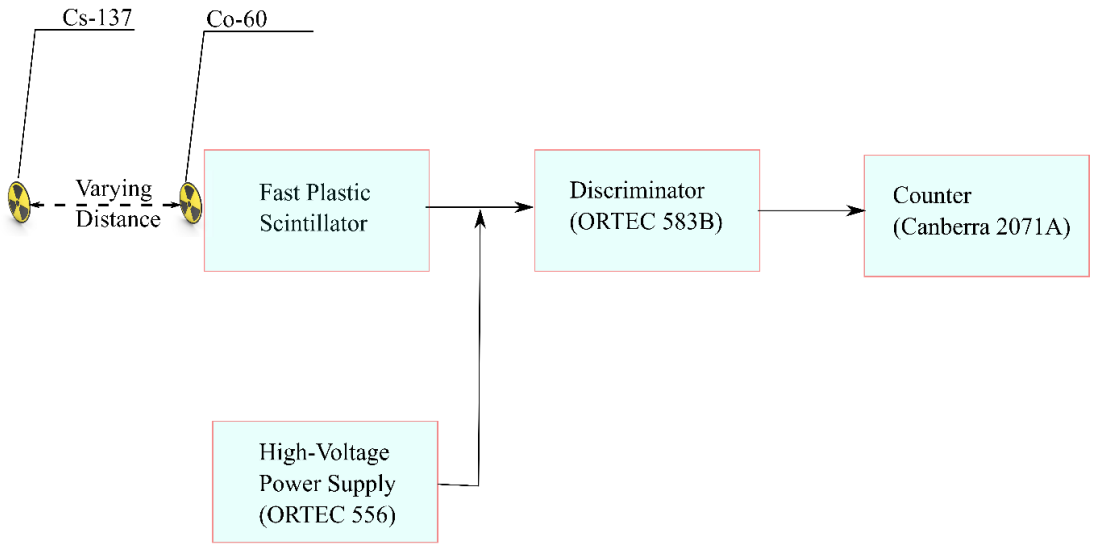

Figure 2. Experimental setup. The sources, ^{60}Co and ^{137}Cs, were placed in front of a fast plastic scintillator detector. Pulse processing was performed using a constant fraction discriminator and counter.

2.2. FLUX RATIO CALCULATIONS

The ratio of ^{60}Co photon flux to that of ^{137}Cs was used as the first independent variable to investigate detection sensitivity. The ^{60}Co flux was calculated from the solid angle (Ω) subtended by the detector face using Eq. (1). The fraction, f_Ω, of emitted photons incident on the detector face is given by Eq. (2):

$$\Omega = 2\pi(1 - cos\theta) \tag{1}$$

$$f_\Omega = \frac{\Omega}{4\pi} = \frac{1-cos\theta}{2} \tag{2}$$

The angle θ is defined by the source-to-detector distance d and detector radius r as shown in Fig. 3. The ^{60}Co/^{137}Cs photon flux ratio, R_f, is defined as:

$$R_f = \frac{A_{\mathrm{Co}} f_{\Omega,\mathrm{Co}}}{A_{\mathrm{Cs}} f_{\Omega,\mathrm{Cs}}} \tag{3}$$

where, A_{Co} and A_{Cs} are the activities of the ^{60}Co and ^{137}Cs sources. Three different photon flux ratios were used. The flux ratio ($f_{\Omega,\mathrm{Cs}}$) was changed using the distance from detector to ^{137}Cs source.

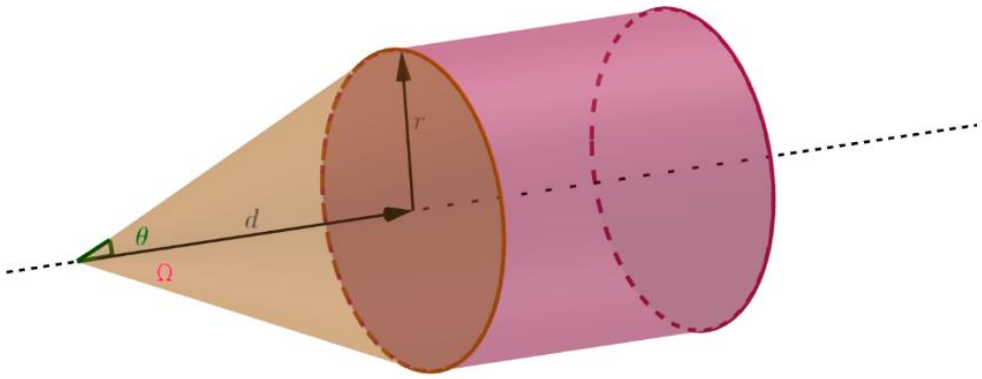

Figure 3. Source and detector geometry.

2.3. DISCRIMINATOR

A low-level discriminator (LLD) was used as a second independent variable to investigate the LOQ. The LLD voltage was swept with the aim of identifying an optimized threshold for the pulse height to separate the lower energy ^{137}Cs pulses from the higher energy ^{60}Co pulses. Here, the final goal was to reduce the LOQ for the higher energy photons. The uncertainty associated with the count rate was based on the Poisson distribution. The measurement error introduced by the LLD dial was assumed to follow a uniform distribution [7]. Uncertainties reported in the Results and Discussion section represent one standard error (1σ).

3. RESULTS AND DISCUSSION

Variation of the ^{60}Co and ^{137}Cs count rates with LLD voltage are shown in Fig. 3. Fig 3a corresponds to an $R_f = 7.3 \times 10^{-2}$, which implies that approximately 7% of the photons incident on the detector are from ^{60}Co. Even at the lowest LLD setting (0.06 V), there is a good separation of the ^{60}Co and ^{137}Cs photons. Between the LLD setting of 0.08 V and 0.1 V, the count rates for the ^{60}Co photons are two orders of magnitude greater than that of ^{137}Cs photons. Fig 3b corresponds to an $R_f = 7.12 \times 10^{-3}$ (~0.7% ^{60}Co). In this case, the optimal threshold for a LLD was about 0.1 V. In Fig 3c, where $R_f = 1.79 \times 10^{-3}$ (~0.2% ^{60}Co), the optimal threshold was also about 0.1 V. But here, the count rate was dominated by the lower energy ^{137}Cs photons. At the higher LLD settings, the count rates for both sources decreased to the background count rate. This implies that the ability to discriminate between the low-activity-high-energy signal counts and the high-activity-low-energy background counts was lost. Thus, it seems that the LLD voltage can be optimized to improve the separation of the low-activity-high-energy photons from the high-activity-low-energy photons. For this experiment, the optimal LLD voltage was around 0.1 V, but it should be noted that the optimal LLD voltage is a function of the detector size, scintillator material, photomultiplier tube design, bias voltage, and the range of gamma ray energies that are to be separated.

The ratio of ^{60}Co/^{137}Cs counts, R_C, as a function of flux ratio is shown in Fig. 5 and Table 1. The relative improvement in sensitivity can be assessed using Currie's "working" limit of quantification (LOQ) for paired observations [22].

$$L_Q = 14.1\sigma_B = 14.1\sqrt{N_B} \tag{4}$$

where, σ_B is the standard deviation of background counts, N_B. Here the ^{137}Cs source is treated as the background and is assumed to follow Poisson statistics. The number of undiscriminated high-energy photon counts, excluding electronic noise, can be crudely approximated as $R_f N_B$. The LOQ is reached when

$$R_f N_B \approx 14.1\sqrt{N_B} \tag{5}$$

$$N_B = CR_0 t_0 \approx \frac{200}{R_f^2} \tag{6}$$

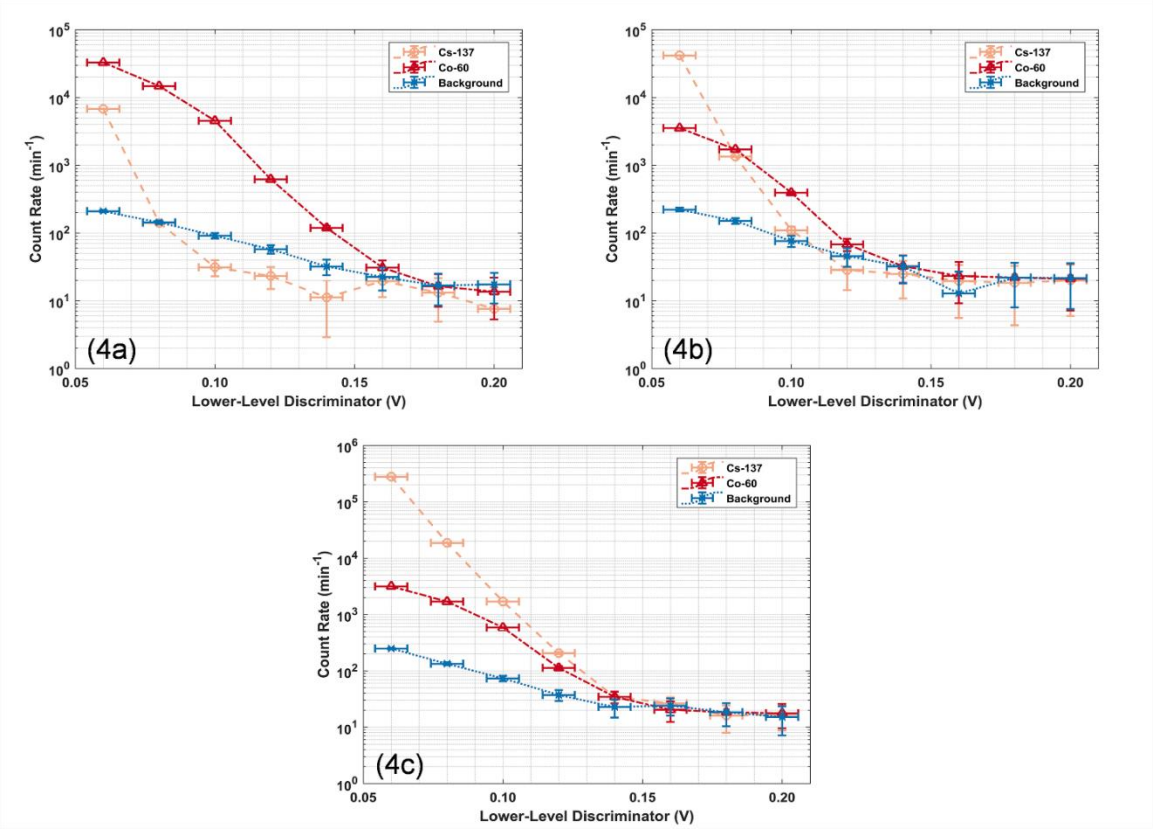

Figure 4. Different Cs-137 source placements and experimental results. (3a) Cs-137 check source placed on the surface of the detector; flux ratio R_f =7.30×10^{-2}; (3b) 38.5 mCi Cs-137 source placed 24 inches away from the detector; flux ratio R_f =7.12×10^{-3}; (3c) 38.5 mCi Cs-137 source placed 12 inches away from the detector; flux ratio R_f =1.79×10^{-3}.

Here, CR_0 is the mean count rate measured without a discriminator (and excluding electronic noise), and t_0 is count time required to reach the LOQ.

When the discriminator is used, R_f should be replaced by R_C, the count ratio,

$$N_B = CR_{LLD}t_{LLD} \approx \frac{200}{R_C^2} \tag{7}$$

CR_{LLD} and t_{LLD} are the count rate and count time to reach the LOQ with the discriminator. A useful metric for the improvement in sensitivity brought about through the use of discrimination is the factor reduction in count time to reach the LOQ.

$$\frac{t_0}{t_{LLD}} = \frac{CR_{LLD}}{CR_0}\frac{R_C^2}{R_f^2} \tag{8}$$

Table 1 also includes estimates of the quantity expressed in Eq. (8). As some unavoidable electronic noise is inherently associated with the measurement of CR_0, counts taken at the lowest LLD setting (0.06 V) were used instead. These results show that pulse height discrimination can improve the sensitivity to the higher-energy photons by several orders of magnitude, at least for R_f values greater than about 0.2% *without sacrificing the short dead time*. However, extrapolating the data also suggests that the improvement in sensitivity may vanish around $R_f \approx 10^{-4}$ suggesting a practical threshold for the method. The optimal threshold might depend on the energy of the signal that has to be discriminated and on the average energy of the background from which the signal has to be discriminated. In this study, ^{60}Co photons (1.173 MeV and 1.332 MeV) were discriminated from ^{137}Cs photons (0.662 MeV). Given a smaller energy gap, one might expect a higher degree of spectral overlap, a reduced ability to discriminate, and a higher threshold for R_f. At the same time, if this technique is to be used to quantify the activity of gamma ray sources in a scattering medium, there is a favorable correlation between the photon flux ratio, R_f, and

the mean energy of the scattered photons. As the source-to-detector distance increases, R_f decreases but the number of Compton scattering mean free paths increases, shifting the scattered spectrum to lower energies and reducing spectral overlap. Future work should be done to investigate the relationship between R_f and pulse-height spectra in greater detail.

Table 1. Flux ratios, count ratios, and reduction in time to reach the limit of quantification (LOQ), LLD=0.1 V.

$^{60}Co/^{137}Cs$ Flux Ratio, R_f	$^{60}Co/^{137}Cs$ Count Ratio, R_C	$\frac{t_0}{t_{LLD}}$
7.30×10^{-2}	145 ± 12	4.8×10^{5}
7.12×10^{-3}	3.6 ± 0.3	3.0×10^{3}
1.79×10^{-3}	0.340 ± 0.007	3.0×10^{2}

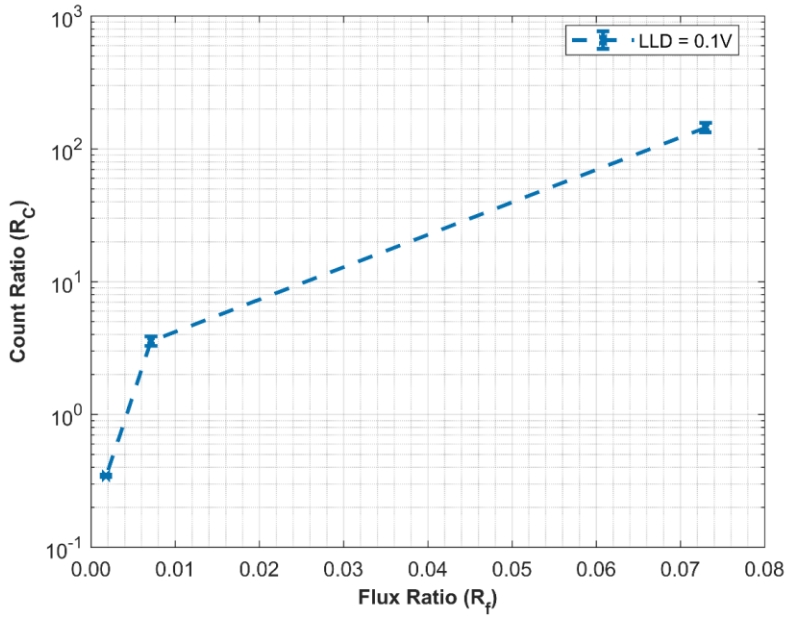

Figure 5. Count ratio (R_C) vs. flux ratio (R_f) at the optimum discriminator setting (LLD=0.1V).

4. CONCLUSIONS

Use of fast plastic scintillators with pulse-height discrimination has been shown to be an effective method to separate pulse counts from low-intensity, high-energy gamma rays from high-intensity, lower-energy gamma rays. Depending on the flux ratio of uncollided-incident to scattered-incident photons, it has been demonstrated that several orders of magnitude decrease in the count time required to reach the limit of detection can be achieved.

ACKNOWLEDGEMENTS

This work was supported by the U.S. Department of Energy, Nuclear Energy University Programs, project 17-13011.

COMPLIANCE WITH ETHICAL STANDARDS

The authors declare that they have no conflict of interest

REFERENCES

1. Artiani PA, Cahyana, Haryanto D, et al (2022) Spent fuel inventories calculation of G.A. Siwabessy Research Reactor 15 MW. IOP Conf Ser Earth Environ Sci 1017:012015.

2. Jacobsson Svärd S, Holcombe S, Grape S (2015) Applicability of a set of tomographic reconstruction algorithms for quantitative SPECT on irradiated nuclear fuel assemblies. Nucl Instrum Methods Phys Res Sect Accel Spectrometers Detect Assoc Equip 783:128–141.

3. Tremsin AS, Craft AE, Bourke MAM, et al (2018) Digital neutron and gamma-ray radiography in high radiation environments with an MCP/Timepix detector. Nucl Instrum Methods Phys Res Sect Accel Spectrometers Detect Assoc Equip 902:110–116.

4. Kotiluoto P, Wasastjerna F, Kekki T, et al (2009) Emission and transmission tomography systems to be developed for the future needs of Jules Horowitz material testing reactor. Nucl Instrum Methods Phys Res Sect Accel Spectrometers Detect Assoc Equip 607:61–63.

5. Kilby S, Fletcher J, Avachat A, et al (2023) Multi-modal tomographic imaging system for poolside characterization of nuclear test fuels: Design considerations and studies. Nucl Instrum Methods Phys Res Sect Accel Spectrometers Detect Assoc Equip 1045:167553.

6. Chernikova D, Axell K, Pázsit I, et al (2013) A direct method for evaluating the concentration of boric acid in a fuel pool using scintillation detectors for joint-multiplicity measurements. Nucl Instrum Methods Phys Res Sect Accel Spectrometers Detect Assoc Equip 714:90–97.

7. Mora MV, Padilla AG, Palomino JLC, Terremoto LAA (2011) Nondestructive burnup measurements by gamma-ray spectroscopy on spent fuel elements of the RP-10 research reactor. Prog Nucl Energy 53:344–353.

8. Aucott TJ, Bandstra MS, Negut V, et al (2014) Effects of Background on Gamma-Ray Detection for Mobile Spectroscopy and Imaging Systems. IEEE Trans Nucl Sci 61:985–991.

9. Aucott TJ, Bandstra MS, Negut V, et al (2015) Impact of detector efficiency and energy resolution on gamma-ray background rejection in mobile spectroscopy and imaging systems. Nucl Instrum Methods Phys Res Sect Accel Spectrometers Detect Assoc Equip 789:128–133.

10. Pérot B (2019) Non-destructive Nuclear Measurements in Support to Nuclear Industry. In: 2019 IEEE Nuclear Science Symposium and Medical Imaging Conference (NSS/MIC). pp 1–4

11. Tsoulfanidis N (2010) Measurement and detection of radiation. CRC press

12. Knoll GF (2010) Radiation detection and measurement. John Wiley & Sons

13. Patil A (2010) Dead time and count loss determination for radiation detection systems in high count rate applications. Missouri University of Science and Technology

14. Thiesse M, Scovell P, Thompson L (2022) Background shielding by dense samples in low-level gamma spectrometry. Appl Radiat Isot 188:110384.

15. Akyurek T (2021) A new dead-time determination method for gamma-ray detectors using attenuation law. Nucl Eng Technol 53:4093–4097.

16. Mrdja D, Bikit K, Bikit I, et al (2019) Optimization of the HPGe detector passive shields by Monte-Carlo simulations. Nucl Instrum Methods Phys Res Sect Accel Spectrometers Detect Assoc Equip 929:76–83.

17. El-Gamal H, Negm H, Hasabelnaby M (2019) Detection efficiency of NaI(Tl) detector based on the fabricated calibration of HPGe detector. J Radiat Res Appl Sci 12:360–366.

18. Hu B, Ye H, Li F-L, et al (2021) New discrimination algorithm for artificial γ radiation sources based on average energy deposition in plastic scintillators. Nucl Instrum Methods Phys Res Sect Accel Spectrometers Detect Assoc Equip 1010:165573.

19. Siciliano ER, Ely JH, Kouzes RT, et al (2005) Comparison of PVT and NaI(Tl) scintillators for vehicle portal monitor applications. Nucl Instrum Methods Phys Res Sect Accel Spectrometers Detect Assoc Equip 550:647–674.

20. Pietryga JM, Padilha LA, Bae WK, et al (2013) Probing the gamma-scintillation process in semiconductor nanomaterials using ultrafast transient cathodoluminescence. In: Chemical, Biological, Radiological, Nuclear, and Explosives (CBRNE) Sensing XIV. SPIE, pp 379–388

21. ASI-100 PLASTIC SCINTILLATOR. In: Alpha Spectra Inc. https://alphaspectra.com/wp-content/uploads/ASI-100-Plastic-Scintillator.pdf. Accessed 12 May 2023

22. Currie LA (1968) Limits for qualitative detection and quantitative determination. Application to radiochemistry. Anal Chem 40:586–593.

III. SUITABILITY OF ANALYTIC TREATMENT OF RADIATION TRANSPORT FOR HIGH RESOLUTION GAMMA RAY COMPUTED TOMOGRAPHY

Zhongmin Jin, Joseph Graham

Missouri University of Science and Technology, 222 Fulton Hall 301 W. 14th St., Rolla, MO, 65401, zj6c6@mst.edu

1. INTRODUCTION

In the nuclear industry, non-destructive testing (NDT) method is playing an important role in characterizing new fuel and materials that are being irradiated in nuclear test reactors. In-pile irradiation experiments are essential for qualifying materials for eventual adoption in advanced reactor designs and the nuclear fuel cycle. NDT methods that aid in characterizing the qualitative and quantitative structural and chemical changes occurring in nuclear fuels under irradiation are sought after [1-4].

Computed tomography (CT) is one of the best tools for non-destructive testing. It takes a few forms: X-ray, gamma and neutron tomography. However, these three tomography techniques have such different interaction modes with materials that their applications would be different. X-rays are suitable for imaging low density materials like soft tissues, plastics. For dense nuclear materials like nuclear fuel and fuel cladding, X-rays are prone to attenuate at a short distance due to their large mass attenuation coefficients and the corresponding low signal-to-noise ratios lower the quality of radiographs. Gamma radiation and X-rays are both the emission of high-energy waves, the main difference lies in that gamma radiation is emitted from the nucleus of an atom. It also has a shorter

wavelength and generally higher energy than X-rays. The higher penetration power is suitable for probing nuclear materials. Even though neutrons do well in imaging fresh and irradiated fuel, they face challenges in a pool-side system where thermal neutrons scattering dominates the transport process. And the mean free path is too short to efficiently detect a practical signal over scattered noise. Secondly, fast neutrons tend to be thermalized in water which leads to a significant loss of spatial resolution. Past studies have used tomographic methods to simulate and experimentally investigate used reactor fuel assemblies. To this end, a proposed submersible gamma-ray computed tomography (CT) system is being designed to eventually perform pool-side fuel characterization at the Advanced Test Reactor (ATR) at Idaho National Laboratories (INL). The purpose of the proposed system is to perform physical, structural, and chemical characterization of irradiated fuel elements from ATR using a combination of emission and transmission CT. Modeling radiation transport of the transmission CT module is the focus of this work.

Many researchers have been using Monte Carlo methods to simulate gamma ray radiation transport. However, these methods could be computationally expensive for a whole set of gamma ray radiographs, especially on personal computers. A Monte Carlo-based approach using variance reduction and analytical correction factors as well as deterministic calculations based on the Beer-Lambert law were compared to analog Monte Carlo calculations that, while physically realistic in terms of geometry and source definition, are too computationally expensive to carry out over the number of projections required to reconstruct a 3D image. These methods of modeling the gamma-ray transmission problem were benchmarked for different collimator geometries to evaluate the range of validity of their assumptions.

2. METHODOLOGY

The Monte Carlo model was developed in the Monte Carlo N-Particle (MCNP6) simulation package [5]. MCNP is a general-purpose Monte Carlo radiation transport code. Fig. 1 shows the cell geometries in the Monte Carlo model of the transmission system. A ^{60}Co source emits intense gamma rays at 1.173 MeV and 1.332 MeV, which are ideal for probing high-Z elements owing to the near-minimum mass attenuation coefficients for most elements at those energies. The ^{60}Co source was defined as a cylindrical volume source in a shielded container. The isotropic source was 1 cm in diameter and 38.1 cm long, with an activity of 2.56×1015 Bq. The size of the cylindrical scintillator crystal was set to 5.08 cm in diameter and 5.08 cm in height, large enough in volume to contain most of the Compton cascade regions within it. A pulse-height tally (F8) was used to determine the spectral response of the detector. A surface flux tally (F2) at the source-facing surface of the scintillator crystal was also used to determine the intensity of incident gamma rays through the collimator and into the detector.

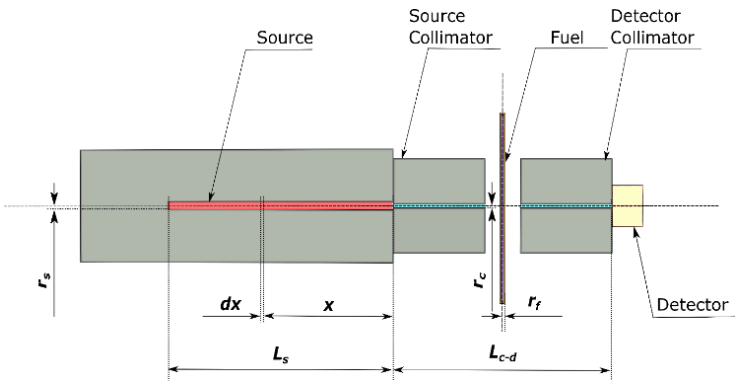

Figure 1. Basic MCNP model of the tomography system with a cylindrical ^{60}Co source. The model consists of: a shielded cylindrical ^{60}Co source, a source collimator, a fuel capsule, a detector collimator, and a LaBr3(Ce) detector.

Deterministic methods have the benefit of less time consumption over conventional Monte Carlo methods. In this proposed tomography system, the Beer-Lambert method was applied to analytically calculate the intensity considering simple exponential attenuation and tabulated mass attenuation coefficients of the materials. Fig. 1 shows the model of the tomography system. The intensity for an uncollided beam of photons is described by the well-known Beer-Lambert law:

$$I(E,x) = I_0(E)e^{-\mu(E)x} \tag{1}$$

where $I(E,x)$ is the intensity of the transmitted radiation beam with photon energy E, $I_0(E)$ is the intensity of the incident beam, $\mu(E)$ is the linear attenuation coefficient of the material, and x is the linear thickness of the material. Eq. 1 assumes gamma rays travel monodirectionally in straight lines. Therefore, the initial intensity used in the Beer-Lambert Law should be adjusted for the solid angle of the detector. A solid angle correction factor is given by

$$f_\Omega(x) = \frac{r_c^2}{4(L_{c-d}+x)^2} \tag{2}$$

where r_c is the radius of the collimator aperture, $L_{c\text{-}d}$ is the distance between the source side of the source collimator and the scintillator side of the detector collimator, and x is the distance between the location where the gamma ray is emitted and the source side of the source collimator. This equation assumes a 1D distribution of isotopically-emitted source particles along the beam axis. As only a fraction of the source volume is within the field-of-view of the detector, a sub-volume correction factor is given by

$$f_{\mathrm{v}} = \frac{\pi r_c^2 Ls}{\pi r_s^2 Ls} \tag{3}$$

$$f_{\mathrm{v}} = \frac{r_c^2}{r_s^2} \tag{4}$$

where rs is the radius of the cylindrical source, Ls is the length of the source. This equation accounts for the large fraction of the source occluded by the collimators from the line-of-sight of the detector. Applying these correction factors to the Beer-Lambert law and integrating over the ^{60}Co source distribution, the intensity of uncollided photons which have passed through the center of the fuel rod and reached the scintillator is given by

$$I(E) = \frac{A_0 r_c^4}{4 L_s r_s^2} \int_0^{L_s} \frac{\exp[-(\mu_s x + 2\mu_f r_f + 2\mu_w L_w)]}{(L_{c-d}+x)^2} dx \quad (5)$$

where A_0 is the activity of the source; L_s is the length of the ^{60}Co source; μ_s, μ_f, and μ_w are the linear attenuation coefficients of the source, fuel rod, and water, respectively; r_f is the radius of the cylindrical fuel; and L_w is the beam path length through the water.

3. RESULTS

Figure 2 demonstrates a plot of Beer-Lambert law results versus MCNP tallies. The MCNP calculation cost 1450 minutes of comfputer time on an hp Z400 workstation. The deterministic took 1 minute on the same workstation. Beer-Lambert calculation focuses on the same location of MCNP F4 tally, and the ratios towards MCNP results at 1.337 MeV are 93%, 86%, 87% for three different collimator aperture diameters (1.0, 1.5, 2.0 cm), respectively. The difference might result from the ideal way to process correction factors without considering the truncated cone beam which still could move towards the detector.

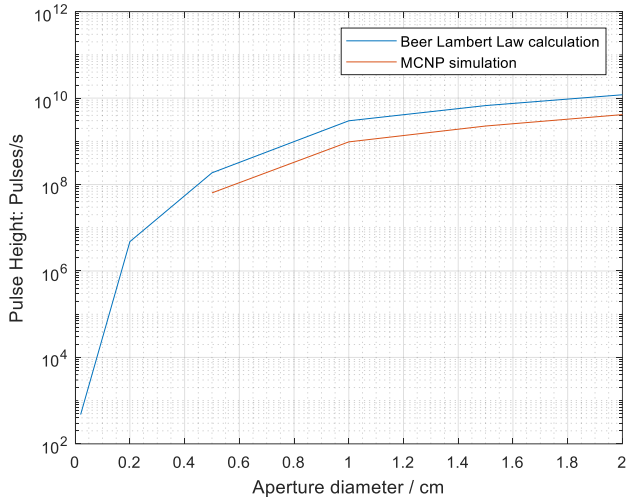

Figure 2. Beer-Lambert law vs. MCNP F8 tally at 1.33 MeV.

REFERENCES

1. De Beer F C (2015) Neutron-and X-ray radiography/tomography: Non-destructive analytical tools for the characterization of nuclear materials. J South Afr Inst Min Metall 115(10):913-924

2. Cesareo R, Brunetti A, Lopes R T, Galli G, Rao D V, Castellano A, Gilardoni M (1999) X-and gamma-ray tomography for nondestructive material testing. Proc SPIE 3772:292-303

3. Jacobsson S, Håkansson A, Jansson P, Bäcklin A (2001) A tomographic method for verification of the integrity of spent nuclear fuel assemblies - II: Experimental investigation. Nucl Technol. 135(2):146-153

4. Jacobsson S, Andersson C, Håkansson A, Bäcklin A (2001) A tomographic method for verification of the integrity of spent nuclear fuel assemblies-I: Simulation studies. Nucl Technol, 135(2):131-145

5. Goorley T, James M, Booth T, Brown F, Bull J, Cox L J, Hendricks J (2012) Initial MCNP6 release overview. Nucl Technol 180(3):298-315

SECTION

2. CONCLUSIONS AND RECOMMENDATIONS

2.1. CONCLUSIONS

To summarize the work accomplished, a series of tasks supporting the design and development of the transmission-CT capabilities of the FIESTA fuel imaging system to be deployed at the Advanced Test Reactor at Idaho National Laboratory. Paper I establishes methods for modeling radiation transport and detector response in the transmission CT detection system. The study compared fully analog MCNP simulations, MCNP simulations with a monodirectionally biased source, and deterministic calculations based on the Beer-Lambert law. Results showed that the monodirectional MCNP simulations were efficient for large collimator aspect ratios and agreed with analog results while deterministic calculations were accurate for semi-quantitative predictions. Both methods allowed the simulation of entire projection radiographs and 3D tomographs. Paper II demonstrates a technique for detecting low-intensity, high-energy gamma rays amidst a high-intensity, low-energy gamma-ray background, utilizing fast plastic scintillators and pulse-height discrimination. Using a ^{60}Co source for the high-energy signal and ^{137}Cs sources to mimic the low-energy background, the research showed that by fine-tuning the low-level discriminator voltage, the sensitivity to high-energy gamma rays can be substantially enhanced. This method is particularly beneficial when detecting high-energy gamma rays in a scattering medium, such as certain nuclear research scenarios. The approach can significantly reduce the time to reach the detection limit, thus improving the efficiency of

gamma-ray detection in complex environments. Moreover, it may reduce the amount of detector shielding needed (and therefore mass) of the system.

In conclusion, this study represents significant progress for nuclear engineering and radiation measurement fields by providing an economically feasible strategy for quantifying uncollided photon flux from highly active sources placed within highly scattering mediums. The implications extend beyond research into industrial applications within nuclear fields. The technique not only enhances detection sensitivity but also efficiently separates low-intensity, high-energy gamma rays from their lower-intensity counterparts amidst complex detection environments. In Paper III, this study discusses the use of analytical treatment in high-resolution gamma-ray computed tomography (CT) for non-destructive testing in the nuclear industry. A submersible gamma-ray CT system was designed for pool-side fuel characterization at the Advanced Test Reactor (ATR) at Idaho National Laboratories. To address the computational expense of Monte Carlo methods for simulating gamma-ray radiation transport, the study introduces a time-efficient deterministic method based on the Beer-Lambert law. Results demonstrate the deterministic model's comparable accuracy and significantly reduced computation time relative to the Monte Carlo methods.

In summary, this doctoral dissertation establishes some of the acquisition parameters in a submersible gamma-ray computed tomography system. This work also identifies some of the unique challenges of acquiring high spatial resolution gamma-ray images in an underwater environment and suggests some ways to reduce deadtime losses. The research findings have important implications for pool-side and in-situ fuel imaging systems.

2.2. RECOMMENDATIONS

Based on the research presented in Paper I and Paper III, there are several suggestions and recommendations for further improvement and exploration:

1. Validation and experimental verification: Validation experiments should be conducted to verify the accuracy and reliability of the proposed modeling techniques, as mentioned in the conclusion. Future work should include experimental validation efforts to demonstrate the effectiveness of developed methods.

2. Sensitivity analysis: Perform a sensitivity analysis to assess how changes in collimator aspect ratio, aperture size, source material, and other system parameters affect the accuracy and efficiency of modeling techniques. This analysis can provide a deeper understanding of system behavior and help identify critical factors that influence results.

3. Expand applicability: While this study focused on a specific submersible 3D gamma-ray computed tomography system for imaging irradiated nuclear fuel, it would be beneficial to explore the applicability of proposed techniques to other CT systems or imaging scenarios by investigating different collimator and detector geometries, energy ranges, and materials.

4. Optimization and parallelization: Explore optimization strategies such as parallelization techniques utilizing high-performance computing resources to accelerate simulations' computational time while enabling larger-scale simulations for real-world applications.

5. Integration with reconstruction algorithms: Consider integrating accelerated modeling techniques with reconstruction algorithms for 3D image reconstruction by

investigating the compatibility between simulation methods and image reconstruction algorithms.

Paper II proposes an effective approach to discriminate high-energy gamma rays from high-activity low-energy backgrounds. Areas for improvement include:

1. Scattering medium variation: The study used ^{137}Cs as a surrogate for a broad spectrum of low-energy scattered photons instead of placing the ^{60}Co source in an actual scattering medium like water. Future research could test the technique in various real-world scattering mediums to see how this impacts results.

2. Pulse height discriminator optimization: The separation of signals depends on the low-level discriminator (LLD) voltage, which varies based on detector size, scintillator material, and photomultiplier tube design. Detailed analysis and optimization of LLD settings may improve spectral separability.

3. Energy gap consideration: Further research is needed on how smaller energy gaps between gamma rays would affect signal discrimination ability since practical scenarios often involve less substantial energy differences than those tested with ^{60}Co and ^{137}Cs gamma rays.

5. Deadtime Analysis: A detailed deadtime analysis under different conditions could provide further insights into optimizing setup performance since detector deadtime has been addressed only generally in the research.

6. Other Fast Scintillator Materials: Other scintillator materials with fast timing characteristics should be tested to determine if they offer any advantages over fast plastic scintillators.

BIBLIOGRAPHY

1. Schulthess J, Woolstenhulme N, Craft A, et al (2020) Non-Destructive post-irradiation examination results of the first modern fueled experiments in TREAT. Journal of Nuclear Materials 541:2. https://doi.org/10.1016/j.jnucmat.2020.152442

2. Senis L (2023) Gamma radiation techniques for non-destructive post-irradiation examination of nuclear fuel: Predicting performance and optimizing instrument design. PhD Thesis, Acta Universitatis Upsaliensis

3. Tremsin AS, Vogel SC, Mocko M, et al (2013) ... & Feller, W. B Non-destructive studies of fuel pellets by neutron resonance absorption radiography and thermal neutron radiography 440:633–646

4. Willman C, Håkansson A, Osifo O, et al (2006) Nondestructive assay of spent nuclear fuel with gamma-ray spectroscopy. Annals of Nuclear Energy 33:427–438. https://doi.org/10.1016/j.anucene.2005.12.005

5. Lehmann EH, Vontobel P, Hermann A (2003) Non-destructive analysis of nuclear fuel by means of thermal and cold neutrons. Nuclear Instruments and Methods in Physics Research, Section A: Accelerators, Spectrometers, Detectors and Associated Equipment 515:745–759. https://doi.org/10.1016/j.nima.2003.07.059

6. Moore GA, Sterbentz DM (2012) Non-Destructive Examination of Fuel Plates for the Rertr Fuel Development Experiments. INL/EXT- 12–27225

7. Montgomery R, Bevard BB, Morris RN, et al ... & Yoon, B. (2018). Sister Rod Nondestructive Examination Final Report (No ORNL/SPR- 2018:

8. Zhang Y, Myhre KG, Bilheux HZ, et al ... & Lin, J. (2023). Non-destructive characterization of advanced nuclear fuel materials using neutron imaging 1014:

9. Preston M, Borella A, Branger E, et al (2021) Analysis of radiation emission from MYRRHA spent fuel and implications for non-destructive safeguards verification. Annals of Nuclear Energy 163:5. https://doi.org/10.1016/j.anucene.2021.108525

10. Kim WK, Lee YW, Cho MS, et al (2008) Nondestructive measurement of the coating thickness for simulated TRISO-coated fuel particles by using phase contrast X-ray radiography. Nuclear Engineering and Design 238:3285–3291. https://doi.org/10.1016/j.nucengdes.2008.07.009

11. Cordes NL, Chuirazzi WC, Kane JJ, Stempien JD (2021) Seeing through nuclear fuel: Three-dimensional, nondestructive X-ray microscopy and volumetric analyses of neutron-irradiated TRISO-coated fuel kernels. MRS Advances 6:1043–1047. https://doi.org/10.1557/s43580-021-00167-1

12. Jansson P, Jacobsson Svärd S, Håkansson A, Bäcklin A (2006) A device for nondestructive experimental determination of the power distribution in a nuclear fuel assembly. Nuclear Science and Engineering 152:76–86. https://doi.org/10.13182/NSE06-A2565

13. Dai Y, Wohlmuther M, Boutellier V, et al (2016) Non-destructive testing of the MEGAPIE target. Journal of Nuclear Materials 468:221–227. https://doi.org/10.1016/j.jnucmat.2015.08.026

14. RICHARDS WJ, MCCLELLAN GC, TOW DM (1982) Neutron Tomography of Nuclear Fuel Bundles. Mater Eval V 40:1263–1267

15. Kamerman D, Cappia F, Wheeler K, et al (2022) Development of axial and ring hoop tension testing methods for nuclear fuel cladding tubes. Nuclear Materials and Energy 31:101175. https://doi.org/10.1016/j.nme.2022.101175

16. Schulthess J, Kamerman D, Winston A, et al (2022) Post-transient examination of performance of uranium silicide fuel and silicon-carbide composite cladding under reactivity-initiated accident conditions. Journal of Nuclear Materials 560:153520. https://doi.org/10.1016/j.jnucmat.2022.153520

17. Senis L, Rathore V, Anastasiadis A, et al (2021) Evaluation of gamma-ray transmission through rectangular collimator slits for application in nuclear fuel spectrometry. Nuclear Instruments and Methods in Physics Research, Section A: Accelerators, Spectrometers, Detectors and Associated Equipment 1014:8. https://doi.org/10.1016/j.nima.2021.165698

18. Kamerman D, Woolstenhulme N, Imholte D, et al (2021) Transient testing of uranium silicide fuel in zircaloy and silicon carbide cladding. Annals of Nuclear Energy 160:108410. https://doi.org/10.1016/j.anucene.2021.108410

19. Cappia F (2020) Non-destructive Examinations of ATF-2 Baseline Rodlets. Idaho National Lab.(INL), Idaho Falls, ID (United States)

20. Pérot B (2019) Non-destructive Nuclear Measurements in Support to Nuclear Industry. In: 2019 IEEE Nuclear Science Symposium and Medical Imaging Conference (NSS/MIC). pp 1–4

21. Vrinda devi KV, Soreng T, Mukherjee D, et al (2010) Non destructive determination of PuO2 content in MOX fuel pins for fast reactors using Passive Gamma Scanning. Journal of Nuclear Materials 399:122–127. https://doi.org/10.1016/j.jnucmat.2010.01.011

22. Virta R, Backholm R, Bubba TA, et al (2020) Fuel rod classification from passive gamma emission tomography (Pget) of spent nuclear fuel assemblies. ESARDA Bulletin 2020

23. Virta R, Bubba TA, Moring M, et al (2022) Improved Passive Gamma Emission Tomography image quality in the central region of spent nuclear fuel. Scientific Reports 12:12473

24. Adam M, Alford R, Barker M, et al (2019) Development of gamma scanning applications in post irradiation examination. book of abstracts, In Proceedings of the fifty sixth annual meeting on hot laboratories and remote handling

25. Kirchknopf P, Almási I, Radócz G, et al (2022) Determining burnup, cooling time and operational history of VVER-440 spent fuel assemblies based on in-situ gamma spectrometry at Paks Nuclear Power Plant. Annals of Nuclear Energy 170:5. https://doi.org/10.1016/j.anucene.2022.108975

26. Patra S, Tripathi R, Pujari PK (2021) Methodology for safeguard and forensics of PHWR spent fuel by gamma-ray spectrometry: a Monte Carlo study. In: Proceedings of the fifteenth biennial DAE-BRNS symposium on nuclear and radiochemistry: book of abstracts

27. Helmreich GW, Kercher AK, Gerczak TJ, et al (2022) Microstructure of irradiated AGR TRISO particle buffer layers as measured by X-ray computed tomography. Journal of Nuclear Materials 572:1. https://doi.org/10.1016/j.jnucmat.2022.154061

28. Wevers M, Kerckhofs G, Pyka G, et al (2012) X-ray computed tomography for nondestructive testing. In: International Conference on Industrial Computed Tomography

29. Davour A, Jacobsson Svärd S, Andersson P, et al (2016) Applying image analysis techniques to tomographic images of irradiated nuclear fuel assemblies. Annals of Nuclear Energy 96:223–229. https://doi.org/10.1016/j.anucene.2016.05.024

30. Jacobsson Svärd S, Holcombe S, Grape S (2015) Applicability of a set of tomographic reconstruction algorithms for quantitative SPECT on irradiated nuclear fuel assemblies. Nuclear Instruments and Methods in Physics Research, Section A: Accelerators, Spectrometers, Detectors and Associated Equipment 783:128–141. https://doi.org/10.1016/j.nima.2015.02.035

31. Jacobsson S, Andersson C, Håkansson A, Bäcklin A (2001) A Tomographic Method for Verification of the Integrity of Spent Nuclear Fuel Assemblies - I: Simulation Studies. Nuclear Technology 135:131–145. https://doi.org/10.13182/NT01-A3211

32. Lowe T, Bradley RS, Yue S, et al (2015) Microstructural analysis of TRISO particles using multi-scale X-ray computed tomography. Journal of Nuclear Materials 461:29–36. https://doi.org/10.1016/j.jnucmat.2015.02.034

33. De Beer FC (2015) Neutron- and X-ray radiography/tomography: Non-destructive analytical tools for the characterization of nuclear materials. Journal of the Southern African Institute of Mining and Metallurgy 115:913–924. https://doi.org/10.17159/2411-9717/2015/v115n10a3

34. Cesareo R, Brunetti A, \ldots RL-D in X, undefined 1999 X-and gamma-ray tomography for nondestructive material testing. spiedigitallibrary.org

35. Jacobsson S, Håkansson A, Jansson P, Bäcklin A (2001) A tomographic method for verification of the integrity of spent nuclear fuel assemblies - II: Experimental investigation. Nuclear Technology 135:146–153. https://doi.org/10.13182/NT01-A3212

36. Yasuda R, Matsubayashi M, Nakata M, et al (2005) Application of neutron imaging plate and neutron CT methods on nuclear fuels and materials. IEEE Transactions on Nuclear Science 52:313–316. https://doi.org/10.1109/TNS.2005.844297

37. Parker HMOD, Joyce MJ (2015) The use of ionising radiation to image nuclear fuel: A review. Progress in Nuclear Energy 85:297–318. https://doi.org/10.1016/j.pnucene.2015.06.006

38. Chichester DL (2012) Demonstration of Computed Tomography to Count Fuel Pins

39. Atak H, Anastasiadis A, Jansson P, et al (2020) The degradation of gamma-ray mass attenuation of UOX and MOX fuel with nuclear burnup. Progress in Nuclear Energy 125:. https://doi.org/10.1016/j.pnucene.2020.103359

40. Dobrin R, Craciunescu T, Tuturici IL (1997) The analysis of failed nuclear fuel rods by gamma computed tomography. Journal of Nuclear Materials 246:37–42. https://doi.org/10.1016/S0022-3115(97)00042-1

41. Holcombe S, Jacobsson Svärd S, Hallstadius L (2015) A Novel gamma emission tomography instrument for enhanced fuel characterization capabilities within the OECD Halden Reactor Project. Annals of Nuclear Energy 85:837–845. https://doi.org/10.1016/j.anucene.2015.06.043

42. Rathore V, Senis L, Andersson Sundén E, et al (2021) Geometrical optimisation of a segmented HPGe detector for spectroscopic gamma emission tomography—A simulation study. Nuclear Instruments and Methods in Physics Research, Section A: Accelerators, Spectrometers, Detectors and Associated Equipment 998:4. https://doi.org/10.1016/j.nima.2021.165164

43. Caruso S (2007) characterisation of high-burnup LWr fueL rods through gamma tomography. Sciences-New York 3762:

44. Hamrashdi HA, Monk SD, Cheneler D (2019) Passive gamma-ray and neutron imaging systems for national security and nuclear non-proliferation in controlled and uncontrolled detection areas: Review of past and current status. Sensors (Switzerland) 19:11. https://doi.org/10.3390/s19112638

45. Brenizer JS (2013) A review of significant advances in neutron imaging from conception to the present. Physics Procedia 43:10–20. https://doi.org/10.1016/j.phpro.2013.03.002

46. Greulich C, Hughes C, Gao Y, et al (2017) High energy neutron transmission analysis of dry cask storage. Nuclear Instruments and Methods in Physics Research, Section A: Accelerators, Spectrometers, Detectors and Associated Equipment 874:5–11. https://doi.org/10.1016/j.nima.2017.08.014

47. Ziock KP, Caffrey G, Lebrun A, et al (2005) Radiation imaging of dry-storage casks for spent nuclear fuel. IEEE Nuclear Science Symposium Conference Record 2:1163–1167. https://doi.org/10.1109/NSSMIC.2005.1596457

48. Große M, Steinbrück M, Stuckert J, et al (2012) Application of neutron radiography to study material processes during hypothetical severe accidents in nuclear reactors. Journal of Materials Science 47:6505–6512. https://doi.org/10.1007/s10853-011-5553-1

49. Gürsoy D, De Carlo F, Xiao X, Jacobsen C (2014) TomoPy: A framework for the analysis of synchrotron tomographic data. Journal of Synchrotron Radiation 21:1188–1193. https://doi.org/10.1107/S1600577514013939

50. Diaz J, Kim T, Petrov V, Manera A (2021) X-ray and gamma-ray tomographic imaging of fuel relocation inside sodium fast reactor test assemblies during severe accidents. Journal of Nuclear Materials 543:152567. https://doi.org/10.1016/j.jnucmat.2020.152567

51. Fu J, Tan R, Wang Q, et al (2012) A cone beam computed tomography inspection method for fuel rod cladding tubes. Nuclear Instruments and Methods in Physics Research Section A: Accelerators, Spectrometers, Detectors and Associated Equipment 688:1–6. https://doi.org/10.1016/j.nima.2012.05.093

52. Fu J, Wang J, Guo W, Peng P (2018) Multi-mounted X-ray cone-beam computed tomography. Nuclear Instruments and Methods in Physics Research Section A: Accelerators, Spectrometers, Detectors and Associated Equipment 888:119–125. https://doi.org/10.1016/j.nima.2018.01.044

53. Saravanan T, Arunmuthu K, Lahiri BB, et al (2015) Dimensional measurements on 112GWd/t irradiated MOX fuel pins using X-ray radiography. Annals of Nuclear Energy 83:8–13. https://doi.org/10.1016/j.anucene.2015.04.005

54. Yuan G, Forna-Kreutzer JP, Xu P, et al (2023) In situ high-temperature 3D imaging of the damage evolution in a SiC nuclear fuel cladding material. Materials & Design 227:111784. https://doi.org/10.1016/j.matdes.2023.111784

55. Arregui-Mena JD, Koyanagi T, Cakmak E, et al (2022) Qualitative and quantitative analysis of neutron irradiation effects in SiC/SiC composites using X-ray computed tomography. Composites Part B: Engineering 238:109896. https://doi.org/10.1016/j.compositesb.2022.109896

56. Liu X, Lee HK (2016) A simulation study of the spent nuclear fuel cask condition evaluation using high energy X-ray computed tomography. NDT & E International 80:58–64. https://doi.org/10.1016/j.ndteint.2016.02.008

57. Endrizzi M (2018) X-ray phase-contrast imaging. Nuclear Instruments and Methods in Physics Research Section A: Accelerators, Spectrometers, Detectors and Associated Equipment 878:88–98. https://doi.org/10.1016/j.nima.2017.07.036

58. Burvall A, Lundström U, Takman PAC, et al (2011) Phase retrieval in X-ray phase-contrast imaging suitable for tomography. Opt Express, OE 19:10359–10376. https://doi.org/10.1364/OE.19.010359

59. Olivo A, Castelli E (2014) X-ray phase contrast imaging: From synchrotrons to conventional sources. Riv Nuovo Cim 37:467–508. https://doi.org/10.1393/ncr/i2014-10104-8

60. Zhu P, Zhang K, Wang Z, et al (2010) Low-dose, simple, and fast grating-based X-ray phase-contrast imaging. Proceedings of the National Academy of Sciences 107:13576–13581. https://doi.org/10.1073/pnas.1003198107

61. Yang M, Zhang J, Meng F, et al (2013) Denoising method of X-ray phase contrast DR image for TRISO-coated fuel particles. Particuology 11:695–702. https://doi.org/10.1016/j.partic.2012.12.011

62. Zhu L, Ewert U, Xiang X, et al (2019) Synchrotron phase-contrast CT to segment the structure boundaries of a TRISO-coated particle. NDT & E International 103:12–18. https://doi.org/10.1016/j.ndteint.2019.01.003

63. Kane JJ, Marshall DW, Cordes NL, et al (2022) 3D analysis of TRISO fuel compacts via X-ray computed tomography. Journal of Nuclear Materials 565:153745. https://doi.org/10.1016/j.jnucmat.2022.153745

64. (1991) Guidebook on non-destructive examination of water reactor fuel. NDT & E International 24:150. https://doi.org/10.1016/0963-8695(91)90151-R

65. Holcombe S (2014) Gamma Spectroscopy and Gamma Emission Tomography for Fuel Performance Characterization of Irradiated Nuclear Fuel Assemblies

66. Lee C, Kim HR (2021) Gamma-Ray Sensor Using YAlO3(Ce) Single Crystal and CNT/PEEK with High Sensitivity and Stability under Harsh Underwater Conditions. Sensors (Basel) 21:1606. https://doi.org/10.3390/s21051606

67. Zeng GL (2010) Transmission and Emission Tomography. In: Zeng GL (ed) Medical Image Reconstruction: A Conceptual Tutorial. Springer, Berlin, Heidelberg, pp 67–85

68. Agency IAE (2022) IAEA Nuclear Safety and Security Glossary. International Atomic Energy Agency

69. Vetter K, Barnowksi R, Haefner A, et al (2018) Gamma-Ray imaging for nuclear security and safety: Towards 3-D gamma-ray vision. Nuclear Instruments and Methods in Physics Research Section A: Accelerators, Spectrometers, Detectors and Associated Equipment 878:159–168. https://doi.org/10.1016/j.nima.2017.08.040

70. Agency IAE (2003) Guidelines for Radioelement Mapping Using Gamma Ray Spectrometry Data. International Atomic Energy Agency

71. Radiation and Shipping Port Security | US EPA. https://www.epa.gov/radtown/radiation-and-shipping-port-security. Accessed 12 Jul 2023

72. Gilmore G (2008) Practical Gamma-ray Spectroscopy. John Wiley & Sons

73. Bieberle A, Hoppe D, Schleicher E, Hampel U (2011) Void measurement using high-resolution gamma-ray computed tomography. Nuclear Engineering and Design 241:2086–2092. https://doi.org/10.1016/j.nucengdes.2011.03.028

74. Kok HV, van der Hagen THJJ, Mudde RF (2001) Subchannel void-fraction measurements in a 6 × 6 rod bundle using a simple gamma-transmission method. International Journal of Multiphase Flow 27:147–170. https://doi.org/10.1016/S0301-9322(00)00005-7

75. Sawicka BD, Murphy RV, Tosello G, et al (1990) Computed tomography of radioactive objects and materials. Nuclear Instruments and Methods in Physics Research Section A: Accelerators, Spectrometers, Detectors and Associated Equipment 299:468–479

76. Adams R, Diaz J, Petrov V, Manera A (2021) Simulation and experiments on the feasibility of using gamma tomography for void fraction measurements in nuclear fuel bundle mock-ups. Annals of Nuclear Energy 154:108073. https://doi.org/10.1016/j.anucene.2020.108073

77. Ahn T, Diaz J, Adams R, et al (2023) Measurement of Local Void Fraction of Air Water Flow in the 8 × 8 Rod Bundle Using High-Resolution Gamma-Ray Tomography. Nuclear Technology 0:1–16. https://doi.org/10.1080/00295450.2023.2197680

78. Fukuchi T, Takeda S, Katsuragawa M, et al (2023) Gamma-ray computed tomography system with a double-sided strip detector. J Inst 18:P01030. https://doi.org/10.1088/1748-0221/18/01/P01030

79. Al-Juwaya T, Ali N, Al-Dahhan M (2017) Investigation of cross-sectional gas-solid distributions in spouted beds using advanced non-invasive gamma-ray computed tomography (CT). Experimental Thermal and Fluid Science 86:37–53. https://doi.org/10.1016/j.expthermflusci.2017.03.029

80. Ong BC, Gupta P, Youssef A, et al (2009) Computed tomographic investigation of the influence of gas sparger design on gas holdup distribution in a bubble column. Industrial and Engineering Chemistry Research 48:58–68. https://doi.org/10.1021/ie800516s

81. Sultan AJ, Sabri LS, Al-Dahhan MH (2018) Investigating the influence of the configuration of the bundle of heat exchanging tubes and column size on the gas holdup distributions in bubble columns via gamma-ray computed tomography. Experimental Thermal and Fluid Science 98:68–85. https://doi.org/10.1016/j.expthermflusci.2018.05.005

82. Qi B, Farid O, Uribe S, Al-Dahhan M (2020) Maldistribution and dynamic liquid holdup quantification of quadrilobe catalyst in a trickle bed reactor using gamma-ray computed tomography: Pseudo-3D modelling and empirical modelling using deep neural network. Chemical Engineering Research and Design 164:195–208. https://doi.org/10.1016/j.cherd.2020.09.024

83. Sabri LS, Sultan AJ, Majdi HS, et al (2022) A Detailed Hydrodynamic Study of the Split-Plate Airlift Reactor by Using Non-Invasive Gamma-Ray Techniques. ChemEngineering 6:. https://doi.org/10.3390/chemengineering6010018

84. Senis L, Rathore V, Andersson P, et al (2023) Performance evaluation of a novel gamma transmission micro-densitometer for PIE of nuclear fuel. Annals of Nuclear Energy 187:109783. https://doi.org/10.1016/j.anucene.2023.109783

85. Caruso S, Murphy MF, Jatuff F, Chawla R (2008) Nondestructive determination of fresh and spent nuclear fuel rod density distributions through computerised gamma-ray transmission tomography. Journal of Nuclear Science and Technology 45:828–835. https://doi.org/10.1080/18811248.2008.9711484

86. Caruso S, Jatuff F (2014) Design, development and utilisation of a tomography station for γ-ray emission and transmission analyses of light water reactor spent fuel rods. Progress in Nuclear Energy 72:49–54. https://doi.org/10.1016/j.pnucene.2013.09.007

87. Farid O, Farzadnia N, Khayat KH, Al-Dahhan M (2022) Feasibility study of implementing gamma-ray computed tomography on measuring aggregate distribution and radiation shielding properties of concrete samples. Construction and Building Materials 327:127034. https://doi.org/10.1016/j.conbuildmat.2022.127034

88. Greulich CR (2018) Radiography of Dry Cask Storage for Used Nuclear Fuel. Christopher Greulich

89. Honkamaa T, Levai F, Turunen A, et al (2014) A prototype for passive gamma emission tomography. IAEA Safeguards Symposium 2015:440

90. Andersson P, Holcombe S (2017) A computerized method (UPPREC) for quantitative analysis of irradiated nuclear fuel assemblies with gamma emission tomography at the Halden reactor. Annals of Nuclear Energy 110:88–97. https://doi.org/10.1016/j.anucene.2017.06.025

91. Andersson P, Holcombe S, Tverberg T (2016) Inspection of a LOCA test rod at the halden reactor project using gamma emission tomography. Top Fuel 2016: LWR Fuels with Enhanced Safety and Performance

92. Hellesen C, Grape S, Jansson P, et al (2017) Nuclear spent fuel parameter determination using multivariate analysis of fission product gamma spectra. Annals of Nuclear Energy 110:886–895. https://doi.org/10.1016/j.anucene.2017.07.035

93. Svärd SJ, Håkansson A, Bäcklin A, et al (2005) Nondestructive experimental determination of the pin-power distribution in nuclear fuel assemblies. Nuclear Technology 151:70–76. https://doi.org/10.13182/NT05-A3632

94. Caruso S, Murphy MF, Jatuff F, Chawla R (2009) Determination of within-rod caesium and europium isotopic distributions in high burnup fuel rods through computerised gamma-ray emission tomography. Nuclear Engineering and Design 239:1220–1228. https://doi.org/10.1016/j.nucengdes.2009.02.019

95. Hsue ST, Crane TW, Talbert J, Lee JC (1978) Nondestructive assay methods for irradiated nuclear fuels. Los Alamos National Lab. (LANL), Los Alamos, NM (United States)

96. Perot B, Jallu F, Passard C, et al (2018) The characterization of radioactive waste: a critical review of techniques implemented or under development at CEA, France. EPJ Nuclear Sciences & Technologies 4:3. https://doi.org/10.1051/epjn/2017033

97. Nett B, PhD (2020) X- Ray Resolution (PSF, MTF, NPS, DQE) For Radiologic Technologists • How Radiology Works. https://howradiologyworks.com/x-ray-resolution/. Accessed 25 Jun 2023

98. Wolbarst AB (2005) Physics of Radiology, 2nd Edition, 2nd edition. Medical Physics Pub Corp, Madison, Wis

99. Knoll GF (2010) Radiation detection and measurement. John Wiley & Sons

100. Tsoulfanidis N (2010) Measurement and detection of radiation. CRC press

101. Kim C, Lee W, Melis A, et al (2021) A Review of Inorganic Scintillation Crystals for Extreme Environments. Crystals 11:669. https://doi.org/10.3390/cryst11060669

102. Kanemitsu Y, Chernyak D, Ejiri H, et al (2020) Purification of the NaI(Tl) crystal for dark matter search project PICOLON. Journal of Physics: Conference Series 1468:012054. https://doi.org/10.1088/1742-6596/1468/1/012054

103. Taheri A, Askari M (2022) Monte Carlo study of plastic rod scintillators for use in industrial computed tomography. Journal of Instrumentation 17:. https://doi.org/10.1088/1748-0221/17/01/P01025

104. Santorelli R, Garcia ES, Abia PG, et al (2021) Spectroscopic analysis of the gaseous argon scintillation with a wavelength sensitive particle detector. Eur Phys J C 81:622. https://doi.org/10.1140/epjc/s10052-021-09375-3

105. Myronov M, Kycia J, Waldron P, et al (2023) Holes Outperform Electrons in Group IV Semiconductor Materials. Small Science 3:2200094. https://doi.org/10.1002/smsc.202200094

106. Wang B, Harris TR, Hogsed MR, et al (2019) Comparison study of temperature dependent direct/indirect bandgap emissions of Ge1-x-ySixSny and Ge1-ySny grown on Ge buffered Si. Thin Solid Films 673:63–71. https://doi.org/10.1016/j.tsf.2019.01.022

107. Stanley CJ, Marshall FM, Advanced Test Reactor: A (2008) National Scientific User Facility. In: Proc. 16th International Conference on Nuclear Engineering. Orlando, FL, United States

108. Kilby S, Fletcher J, Avachat A, et al (2023) Multi-modal tomographic imaging system for poolside characterization of nuclear test fuels: Design considerations and studies. Nuclear Instruments and Methods in Physics Research Section A: Accelerators, Spectrometers, Detectors and Associated Equipment 1045:167553. https://doi.org/10.1016/j.nima.2022.167553

109. Vo NT, Atwood RC, Drakopoulos M, Connolley T (2021) Data processing methods and data acquisition for samples larger than the field of view in parallel-beam tomography. Optics Express 29:17849. https://doi.org/10.1364/oe.418448

110. Kilby S, Jin Z, Avachat A, et al (2019) A source biasing and variance reduction technique for Monte Carlo radiation transport modeling of emission tomography problems. Journal of Radioanalytical and Nuclear Chemistry 320:37–45. https://doi.org/10.1007/s10967-019-06457-1

111. Kilby S, Fletcher J, Jin Z, et al (2021) Comparison of a semi-analytic variance reduction technique to classical Monte Carlo variance reduction techniques for high aspect ratio pencil beam collimators for emission tomography applications. Nuclear Instruments and Methods in Physics Research, Section A: Accelerators, Spectrometers, Detectors and Associated Equipment 1001:. https://doi.org/10.1016/j.nima.2021.165236

112. Goorley T, James M, Booth T, et al (2012) Initial MCNP6 Release Overview. Nuclear Technology 180:298–315. https://doi.org/10.13182/NT11-135

113. Berger MJ, Hubbell JH, Seltzer SM, et al (2010) XCOM: Photon Cross Section Databese (version 1.5). 2010:

114. Chadwick MB, Obložinský P, Herman M, et al (2006) ENDF/B-VII. 0: next generation evaluated nuclear data library for nuclear science and technology. Nuclear data sheets 107:2931–3060. https://doi.org/10.1016/j.nds.2006.11.001

115. MacFarlane RE, Kahler AC (2010) Methods for Processing ENDF/B-VII with NJOY. Nuclear Data Sheets 111:2739–2890. https://doi.org/10.1016/j.nds.2010.11.001

116. Jin Z, Kilby S, Avachat A, et al (2022) Accelerated radiation transport modeling techniques for pencil beam computed tomography using gamma rays. Nuclear Instruments and Methods in Physics Research Section A: Accelerators, Spectrometers, Detectors and Associated Equipment 1039:167165. https://doi.org/10.1016/j.nima.2022.167165

VITA

Zhongmin Jin was born in Yanling, China and later moved to Beijing. He obtained his M.S. degree in Nuclear Engineering from North China Electric Power University in 2011 and received an award for his outstanding research achievements on behalf of the Nuclear Engineering department at the 6th “Electric Science & Technology” Cup. Prior to joining the Ph.D. program at Missouri University of Science and Technology with Dr. Joseph Graham in fall 2017, he worked as an engineer at State Nuclear Power Research Institute (SNPRI). During his time there, he focused on preliminary advanced reactor concept design and reactor physics simulations.

Zhongmin Jin successfully defended his doctoral dissertation in July 2023 and received his Ph.D. in Nuclear Engineering in December 2023 from Missouri University of Science and Technology.